Cohesive Crack Models and Finite Fracture Mechanics analytical solutions for FRP-concrete single-lap shear test: An overview

Cohesive Crack Models and Finite Fracture Mechanics analytical solutions for FRP-concrete single-lap shear test: an overview

P. Cornetti[(1)], M. Muñoz-Reja[(2)], V. Mantič[(2)]

(1) Department of Structural, Geotechnical and Building Engineering, Politecnico di Torino, Corso Duca degli Abruzzi 24, 10129 Torino, Italy

(2) Grupo de Elasticidad y Resistencia de Materiales, Escuela Técnica Superior de Ingeniería, Universidad de Sevilla, Camino de los Descubrimientos s/n, 41092 Sevilla, Spain

Abstract. In the present paper we review and compare several analytical models describing the single-lap shear test, which is the most common test to determine the bonding behaviour between a strengthening FRP plates and the concrete substrate. The models are one-dimensional and formulated under the assumption that debonding occurs as a pure mode II cracking process throughout a zero-thickness interface between the FRP strip and the brittle substrate. As such, they are all amenable of an analytical treatment. The FRP-concrete interface is described by at most three parameters among the interfacial fracture energy, the tensile strength and the elastic stiffness. Particularly, we compare the effective bond length estimates provided by different models and compare them with the ones present in Design Codes. Finally, a comparison with experimental data sets available in the Scientific Literature is also given.

Keywords: Fibre-reinforced polymer (FRP); Debonding; Effective bond length; Finite Fracture Mechanics; Cohesive zone models; Bond-slip model

1. Introduction

Strengthening of concrete or masonry structures by externally bonded Fiber Reinforced Polymer (FRP) plates is nowadays a popular technique. In order to assess the strength of the reinforced structure, investigating the bond behaviour between the existing structure and the reinforcement is a matter of primary concern. From an experimental point of view, the bonding is investigated mainly by means of the single-lap shear test (sometime called also pull-push test), where the FRP is pulled away from a pushed concrete substrate prism.

The two main peculiar features of externally bonded reinforcements are: (i) the existence of a threshold value for the load that can be transferred from the reinforcement to the support, whatever the reinforcement strength is, and (ii) the existence of an effective length, i.e. a bond length beyond which there is no significant increase of the transferable load. It means that, beyond a certain level, it makes no sense to use a stronger reinforcement since delamination will prevail on reinforcement failure. This is a fundamental difference with respect to inner reinforcements, where, due to friction, it always exists an embedment length allowing the complete exploitation of the reinforcement strength.

A huge literature exists about the single-lap shear test, focusing on its theoretical, numerical and experimental aspects. Among the most comprehensive review papers, in chronological order, we can cite the ones by Chen & Teng (2001), Lu et al. (2005), Dai et al. (2006), Wu & Jiang (2013), D'Antino & Pellegrino (2014), Vaculik et al. (2018a).

For the single-lap shear test of an FRP plate from a brittle substrate, peeling stresses are usually negligible. Recent results by Muñoz-Reja et al. (2020a), where the role of peeling stresses in single-

lap shear test was thoroughly studied, confirmed this early conjecture. Thus, shear-lag models are enough to catch the basic features of the debonding process; the problem is typically faced by means of an interface constitutive law linking the shear stresses to the relative longitudinal displacements between the concrete substrate and the FRP (the so-called *bond-slip* law). This approach is a particular application of the Cohesive Crack (or Zone) Model (CCM) to interface debonding. Although we will not consider peeling stresses, it is important to emphasize that, in the case of more general bi-material system configurations, peeling stresses cannot be neglected, so that more complex models accounting for mixed-mode fracture are required for simulating such geometries. We refer the reader to the papers by Ascione & Mancusi (2010) and by Zhang et al. (2021), both focusing on mixed-mode debonding by coupling traction-separation and bond-slip cohesive laws, and to the paper by De Maio et al. (2022), where, beyond reinforcement debonding, also the competition with concrete cracking has been addressed.

Among the first paper on the subject, we can cite the pioneering papers by Taljsten (1997), De Lorenzis et al. (2001) and Yuan et al. (2001). For what concerns more specifically analytical modelling, Yuan et al. (2004) provided the full-range solution (i.e. the interface stress evolution from the elastic regime up to complete reinforcement detachment) assuming a bilinear interface constitutive law. The solution by Yuan et al. (2004) holds only for relatively large bond lengths; later, it was extended to relatively short overlap lengths by Cornetti & Carpinteri (2011) and Caggiano et al. (2012) (and recently revisited by Martinelli (2021)). Cornetti & Carpinteri (2011) provided also the analytical solution for an interface constitutive law characterised by an exponential softening branch; the exponential softening model has been later extended to investigate the behaviour under cycling loads by Caggiano & Martinelli (2021) and Bocciarelli (2021). Cornetti et al. (2012) solved the single-lap shear problem by means of the Finite Fracture Mechanics model. Progress in analytical modelling led to improvement and updating of the formulae provided in Technical Standards; for a recent comparison about the effectiveness of the Standards prescriptions, see Monaldo et al. (2019).

Recent one-dimensional analytical modelling approaches for the single-lap shear test followed two different paths. The first research direction focussed the attention on more complex (and closer to experimental data) bond-slip laws. A sudden stress drop at the beginning of the softening branch was considered in Leung & Yang (2006). Bond-slip laws where both the ascending and softening branches are described by a unique function were considered by Ferracuti et al. (2007) – of power-law type – and by Wu et al. (2012) and Biscaia et al. (2016) – of exponential type. Yuan et al. (2012) took into account a bond-slip law with a linear hardening and an exponential softening. The second research direction exploited the simpler linear softening model to investigate particular material and/or phenomena. He et al. (2015) and Zheng et al. (2020) investigated the unloading occurring during the snap back. Colombi & D'Antino (2018), Vaculik et al. (2018b), Zou et al. (2019) and Mirzaei et al. (2021) extended the model to take residual friction into account. Finally, Grande et al. (2019) developed a two-layer model to describe debonding in Fiber Reinforced Cementitious Matrix (FRCM) strengthening systems, while other researchers investigated the FRP debonding from curved substrates (De Lorenzis & Zavarise (2010), Biscaia et al. (2017), Malena (2018)).

For what concerns the present paper, its aim is not to provide more sophisticate models for the single-lap shear test but to present the most common solutions, along with some new ones, in a unified, simple way, to compare them and to check them against experimental data. Comparisons between Cohesive Zone Models can be found in Yuan et al. (2001) for the single-lap shear test, in Alfano et al. (2006) for general interfacial problems and in Malena et al. (2017) for FRP-masonry interfaces; comparisons between Linear Elastic Fracture Mechanics and Cohesive Zone Model for FRP plated concrete beams are available in Rabinovitch (2008) and De Lorenzis & Zavarise (2009). Herein, attention will focus on the determination of the debonding load and of the effective length for the single-lap shear test (Cottone & Giambanco, 2009; Franco & Royer-Carfagni, 2014): analytical (or semi-analytical) expressions will be given according to Linear Elastic Fracture

Mechanics, Linear Elastic Perfectly Brittle Model, Cohesive Zone Models and Finite Fracture Mechanics. In more detail, in Section 2 we will review the following models:

- *One-parameter model:*
  1) Linear Elastic Fracture Mechanics (LEFM)
- *Two-parameter models:*
  2) Linear Elastic Perfectly Brittle Model (LEBIM)
  3) Rigid-Linear Softening Model (R-LSM)
  4) Rigid-Exponential Softening Model (R-ESM)
  5) Equivalent-LEBIM (Eq.-LEBIM)
- *Three-parameter models:*
  6) Finite Fracture Mechanics (FFM)
  7) Linear Elastic-Linear Softening Model (LE-LSM)
  8) Linear Elastic-Exponential Softening Model (LE-ESM).

Recall that LEBIM and Eq.-LEBIM, without softening part, represent a (nonsmooth) limit case of LE-LSM and LE-ESM (often referred to as intrinsic CCMs), whereas R-LSM and R-ESM (often referred to as extrinsic CCMs), represent another limit cases of intrinsic CCMs, LE-LSM and LE-ESM, respectively, without the initial linear elastic part. Moreover, note that, prior to an interface damage appears, a perfect interface, without any relative displacement at the interface, is considered in LEFM, R-LSM and R-ESM, whereas in the other models there is a linear elastic relation between interface tractions and relative interface displacements.

By means of a proper dimensionless formulation, it is possible to obtain:

(i) a unique curve providing the debonding load vs. the bond length for the two-parameter models and

(ii) a family of curves depending on a unique parameter for the three-parameter models.

Each curve provides a different expression for the effective bond length.

In Section 3 a discussion about the different estimates for the effective bond length obtained in Section 2 will be provided along with comparisons with some experimental data from the Literature. Finally, conclusions will be drawn in Section 4.

Although, in the Authors' opinion, the main quality of the present paper is a synoptic presentation of the different models, some of the formulae proposed in the paper are original (as well as the comparison with experimental data sets from Literature), especially for what concerns the three-parameter models and the effective bond lengths.

2. The single-lap shear test

The single-lap shear test is one of the most common experimental tests to evaluate the bond between FRP and concrete and a huge literature is available about it. In the test, an FRP plate is glued by means of an adhesive layer at the top of a concrete block (Fig.1). One edge of the FRP strip is pulled (i.e. under traction) while the concrete block is pushed by means of a reaction frame (i.e. compressed). If the reinforcement is sufficiently strong, failure is usually achieved by its debonding from the block. Typical output of the single-lap shear test is the FRP load vs. displacement (at loaded end) plot; the maximum load value achieved during the test represents the failure (or debonding) load.

Referring to Fig.1, the width and thickness of the reinforcement plate are denoted respectively by t_r and h_r, those of the concrete block by t_b and h_b, and the bonded length is l; x is the longitudinal coordinate. Young's moduli of plate and concrete are E_r and E_b respectively. G_a and G_b are the shear elastic moduli of the adhesive and of the concrete. Finally, h_a is the adhesive layer thickness.

In what follows we will provide the debonding load F_c according to different models and highlight (if any) the value of the effective bond length.

2.1. LEFM

Let us start assuming a perfectly brittle and infinitely rigid interface between the FRP and the concrete block (LEFM model). Accordingly, the failure load is achieved by means of the Griffith (infinitesimal) energy balance. Delamination occurs when the crack driving force $\mathcal{G}$ reaches the fracture energy $\mathcal{G}_c$:

$$\mathcal{G} = \frac{1}{t_r}\frac{d\phi}{da} = \mathcal{G}_c \tag{1}$$

where a is the crack length and da the infinitesimal crack increment, while ϕ is the strain energy and dϕ (at fixed load) is the strain energy variation after and before crack propagation (see Fig.2). Outside the region $l-(a+da)<x<l-a$, the stress-strain state in the reinforcement and concrete block remains unchanged and hence there is no variation in the strain energy. Within the same region the overall axial force is zero; thus, the strain energy in the strip is null before crack advance. Therefore:

$$d\phi = \frac{F_c^2}{2E_r h_r t_r}da + \frac{F_c^2}{2E_b h_b t_b}da \tag{2}$$

From Eqs. (1) and (2) the critical load can be obtained as:

$$F_c = t_r\sqrt{\frac{2\mathcal{G}_c E_r h_r}{1+\rho}} \tag{3}$$

where ρ is the mechanical fraction of reinforcement (i.e. $\rho = E_r t_r h_r / E_b t_b h_b$). It is evident that, according to LEFM, the debonding load F_c does not depend on the bond length. This feature is contradicted by experiments (and by more refined models), where an *effective* bond length (larger than zero) exists: above this length there is no significant load increment, below this length the debonding load decreases. Nevertheless, the present result is important since the value (3) represents the maximum transferable force, attained for sufficiently large (or infinite) bond lengths, according to all the subsequent models we are considering. For this reason, the (asymptotical) value (3) is hereafter marked as F_c^∞. Finally, note that in Literature and Standards reference is usually made to the critical load value:

$$F_c = t_r\sqrt{2\mathcal{G}_c E_r h_r} \tag{4}$$

which can be seen as a particular case of the previous one if the elasticity of the concrete substrate is neglected ($\rho = 0$). Of course, for large concrete blocks and/or thin reinforcements, the values (3) and (4) almost coincide.

Finally, for what concerns the $\mathcal{G}_c$ value, it is worth observing that usually delamination cracks run few millimetres under the concrete skin. Hence, $\mathcal{G}_c$ is a *concrete* material property. In absence of a suitable experimental value, standards like CNR-DT 200 R1/2013 (2013) provide an empirical relationship correlating the fracture energy to the concrete tensile and compression strength.

LEFM is a *one-parameter* model since the interface is characterized by just one parameter, i.e. the fracture energy $\mathcal{G}_c$.

2.2. LEBIM

It is evident that in the single-lap shear test, the interface is mainly subjected to shear deformations; hence, delamination occurs in prevailing mode II conditions. Although a rigorous elastic analysis of the problem shows that also a mode I component is present (see e.g. Suo & Hutchinson 1990, Muñoz-Reja et al. 2020b), henceforth we will neglect peeling stresses since they are relatively low and highly localized for thin reinforcement plates as the FRP ones.

According to the previous considerations, a simple (i.e. Volkersen) mechanical model for the single-lap shear test can be established by treating the plate and the concrete prism (the two

adherents) as being subjected to axial deformations only, while the adhesive layer (i.e. the interface) can be assumed to be subjected to shear deformations only. That is, both adherents are assumed to be subjected to uniformly distributed axial stresses, with any bending effects neglected, while the adhesive layer is modelled by a proper shear stress vs. relative longitudinal displacement constitutive law (bond-slip relationship). Note that the assumption of uniformly distributed axial stress is valid if the relative difference between the width of the concrete block and of the reinforcement is not too high (t_r / t_b larger than about 0.5).

Based on the previous assumptions, the equilibrium equations of the reinforcement and of the overall cross section read respectively:

$$h_r \frac{d\sigma_r}{dx} - \tau = 0 \tag{5}$$

$$\sigma_r h_r t_r + \sigma_b h_b t_b = 0 \tag{6}$$

where τ is the shear stress in the adhesive layer, σ_r is the axial stress in the reinforcement plate and σ_b is the axial stress in the concrete prism. Assuming a linear-elastic behaviour for the adherents, the constitutive equations read:

$$\tau = \tau(s), \quad \sigma_r = E_r \frac{du_r}{dx}, \quad \sigma_b = E_b \frac{du_b}{dx} \tag{7}$$

where u_r and u_b are the longitudinal displacements of the reinforcement and of the concrete, respectively, and s is the interfacial slip, defined as the relative displacement between the two adherents (i.e. $s = u_r - u_b$). By means of Eqs. (5-7), it is possible to achieve the following second order differential equation in s:

$$\frac{d^2 s}{dx^2} - \frac{1+\rho}{E_r h_r} \tau(s) = 0 \tag{8}$$

By some analytical manipulations, the stress in the FRP can be expressed as a function of the first derivative of the slip:

$$\sigma_r = \frac{E_r}{1+\rho} \frac{ds}{dx} \tag{9}$$

Accordingly, the force F at the loaded end can be evaluated as:

$$F = t_r h_r \sigma_r(l) = \frac{E_r t_r h_r}{1+\rho} \left. \frac{ds}{dx} \right|_{x=l} \tag{10}$$

or, equivalently, as:

$$F = t_r \int_0^l \tau(x)\, dx \tag{11}$$

Equations from (5) up to (11) hold for all the models presented hereafter.

On the other hand, Linear Elastic Brittle Interface Model (LEBIM, e.g. Bennati et al (2009), Távara et al. (2010, 2011), Mantič et al. (2015)) is achieved by assuming (Fig. 3a) a linear elastic-perfectly brittle behaviour for the interface:

$$\tau(s) = \begin{cases} k\, s, & \text{for} \quad 0 \le s \le s_{f0} \\ 0, & \text{for} \quad s > s_{f0} \end{cases} \tag{12}$$

where k is the stiffness of the interface, which hence can be seen as a bed of linear elastic springs. The area beneath the τ-s relationship is the fracture energy $\mathcal{G}_c$; hence the displacement value at which the stress drops to zero, i.e. is $s_{f0} = \sqrt{2\mathcal{G}_c / k}$. It is evident that LEBIM is a *two-parameter* model, since the interface is completely described by two parameters, i.e. $\mathcal{G}_c$ and k. The peak stress is equal to $\sqrt{2k\mathcal{G}_c}$; as such, it is not a free quantity but depends on k and $\mathcal{G}_c$.

The shear deformability (i.e. the compliance) of the interface is the sum of the deformability (G_a/h_a) of the adhesive layer and the one (G_b/h_{bi}) of the concrete layer (of thickness h_{bi}) contributing

to the overall shear deformability of the FRP-concrete junction. Hence, the shearing elastic stiffness of the interface can be estimated as:

$$k = \frac{1}{\frac{h_a}{G_a} + \frac{h_{bi}}{G_b}} \tag{13}$$

In absence of suitable experimental data, Italian Standards (CNR-DT 200 R1/2013) suggest to use $h_{bi} = 20 \div 30$ mm.

Substituting Eq. (12) into Eq. (8) and exploiting Eqs. (9-10) to set the boundary conditions, we get the differential problem as:

$$\begin{cases} \dfrac{\mathrm{d}^2 s}{\mathrm{d}x^2} - \dfrac{1+\rho}{E_r h_r} k\, s = 0 \\ \left.\dfrac{\mathrm{d}s}{\mathrm{d}x}\right|_{x=0} = 0 \\ \left.\dfrac{\mathrm{d}s}{\mathrm{d}x}\right|_{x=l} = \dfrac{(1+\rho)}{E_r t_r h_r} F \end{cases} \tag{14}$$

whose solution reads, for all $0 \le x \le l$:

$$\tau(x) = \frac{F}{t_r}\sqrt{\frac{k(1+\rho)}{E_r h_r}}\,\frac{\cosh\left(x\sqrt{\dfrac{k(1+\rho)}{E_r h_r}}\right)}{\sinh\left(l\sqrt{\dfrac{k(1+\rho)}{E_r h_r}}\right)} \tag{15}$$

It is evident that the maximum is achieved at the loaded end, i.e. $\tau_{max} = \tau(l)$. For LEBIM model the strain energy release rate is the strain energy stored in the spring where crack occurs (see e.g. Krenk, 1992; Lenci, 2001; Mantič et al., 2015): $\mathcal{G} = \tau_{max}^2 / 2k$. Debonding occurs when $\mathcal{G}$ reaches $\mathcal{G}_c$. Therefore, the debonding load is given by:

$$F_c = F_c^{\infty} \tanh\left(l\sqrt{\frac{k(1+\rho)}{E_r h_r}}\right) \tag{16}$$

Eq. (16) is plotted in Fig. 3b in dimensionless form (see next section for the definition of normalized quantities); it clearly shows that LEBIM model is able to catch the increment of the debonding load as the bond length increases. Now we can define the effective bond length as the length value beyond which the debonding load is a fraction β of the maximum achievable one (i.e. $\beta = F_c / F_c^{\infty}$), with β close to unity. Hence, from Eq. (16):

$$l_{eff} = \operatorname{arctanh}(\beta) \times \sqrt{\frac{E_r h_r}{k(1+\rho)}} \tag{17}$$

Assuming, e.g. $\beta = 0.95$, we get:

$$l_{eff} = 1.83 \times \sqrt{\frac{E_r h_r}{k(1+\rho)}} \tag{18}$$

i.e., beyond this value, the LEBIM model predicts a failure load higher than 95% of F_c^{∞}.

Finally note that the LEFM model of Section 2.1 can be seen as a particular case – for an infinitely stiff interface – of the LEBIM one, i.e. LEBIM reverts to LEFM as $k \to \infty$.

2.3. CCM: Rigid-Linear Softening Model (R-LSM)

A more refined model can be achieved by assuming a rigid-linear softening constitutive (cohesive) law for the interface. The reason for such a choice is that experiments usually show the presence of

a softening in the bond-slip law characterizing the interface. Moreover, in the cohesive law, the ascending branch is often smaller than the softening tail, so that, as a first approximation, the interface (elastic) stiffness k (Eq. (13)) can be set equal to infinity. Accordingly, the bond-slip law reads:

$$\tau(s) = \begin{cases} \tau_c(1 - s/s_f), & \text{for} \quad 0 \le s \le s_f \\ 0, & \text{for} \quad s > s_f \end{cases} \tag{19}$$

where τ_c is the (shear) interface strength and s_f is the value of the relative displacement at which cohesive stresses disappear, i.e. the *final relative displacement*. The area beneath the cohesive law is the fracture energy. Thus:

$$s_f = 2\mathcal{G}_c/\tau_c \tag{20}$$

Note that the final relative displacement value provided by Eq. (20) is generally different (and higher) with respect to the value s_{f0} provided in Section 2.2.

As LEBIM model, also the R-LSM model is a *two-parameter* model, since it requires only two parameters to be known: differently from LEBIM, now they are the fracture energy $\mathcal{G}_c$ and the interface strength τ_c.

It is now convenient to introduce a characteristic length l_{ch} defined as the overlap length a joint should have in order to withstand the force F_c^∞ if the interfacial stresses were constant and equal to the shear strength τ_c, i.e. $\tau_c\, t_r l_{ch} = F_c^\infty$. Hence:

$$l_{ch} = \frac{F_c^\infty}{\tau_c t_r} = \frac{1}{\tau_c}\sqrt{\frac{2\mathcal{G}_c E_r h_r}{1+\rho}} \tag{21}$$

Then, we introduce the following dimensionless quantities:

$$\xi = \frac{x}{l_{ch}}, \quad \lambda = \frac{l}{l_{ch}}, \quad \tilde{s} = \frac{s}{s_f}, \quad \tilde{F} = \frac{F}{F_c^\infty}, \quad \tilde{F}_c = \frac{F_c}{F_c^\infty}, \quad \tilde{\tau} = \frac{\tau}{\tau_c} \tag{22}$$

In dimensionless form, Eq. (8) now reads:

$$\frac{\mathrm{d}^2\tilde{s}}{\mathrm{d}\xi^2} - \tilde{\tau}(\tilde{s}) = 0 \tag{23}$$

Eqs. (10-11) read:

$$\left.\frac{\mathrm{d}\tilde{s}}{\mathrm{d}\xi}\right|_{\xi=\lambda} = \tilde{F} \tag{24}$$

$$\int_0^\lambda \tilde{\tau}(\xi)\,\mathrm{d}\xi = \tilde{F} \tag{25}$$

while Eq. (19) becomes (see Fig. 3a):

$$\tilde{\tau}(\tilde{s}) = \begin{cases} 1 - \tilde{s}, & \text{for} \quad 0 \le \tilde{s} \le 1 \\ 0, & \text{for} \quad \tilde{s} > 1 \end{cases} \tag{26}$$

It is clear that the maximum transferable load is achieved when all the bond length is in the softening regime. Upon substitution of Eq. (26) into Eq. (23), the differential problem now reads:

$$\begin{cases} \tilde{s}'' + \tilde{s} = 1 \\ \tilde{s}(0) = 0 \\ \tilde{s}'(0) = 0 \end{cases} \tag{27}$$

since at the left extreme both the relative displacement and the load are null. Its solution yields:

$$\tilde{s} = 1 - \cos\xi \tag{28}$$

$$\tilde{\tau} = \cos\xi \tag{29}$$

$$\tilde{F}_c = \tilde{s}'(\lambda) = \int_0^\lambda \tilde{\tau}(\xi)\mathrm{d}\xi = \sin\lambda \tag{30}$$

Of course, Eqs. (28-30) hold true for $0 \le \xi \le \lambda \le \pi/2$. For $\lambda > \pi/2$ the limit value F_c^∞ is always achieved, i.e. $\tilde{F}_c = 1$. Thus, it is clear that the present model is able to catch the transition from strength-governed failure for short bond lengths:

$$\tilde{F}_c \cong \lambda \quad \Rightarrow \quad F_c \cong \tau_c \times (t_r l) \tag{31}$$

up to energy-driven debonding for large bond lengths:

$$\tilde{F}_c \cong 1 \quad \Rightarrow \quad F_c \cong F_c^\infty = t_r \sqrt{\frac{2\mathcal{G}_c E_r h_r}{1+\rho}} \tag{32}$$

as evident in Fig. 3b. This is a general feature of the CCM and it will hold for all the CCMs presented henceforth.

According to the present model, the effective bond length l_{eff} can be exactly defined as (introducing $\lambda_{eff} = l_{eff} / l_{ch}$):

$$\lambda_{eff} = \frac{\pi}{2} \quad \Rightarrow \quad l_{eff} = \frac{\pi}{2\tau_c} \sqrt{\frac{2\mathcal{G}_c E_r h_r}{1+\rho}} \tag{33}$$

since, beyond this value, F_c is exactly equal to F_c^∞. However, relaxing the condition from $F_c = F_c^\infty$ to $F_c > \beta \times F_c^\infty$ as done above, the effective bond length estimate gets equal to:

$$\lambda_{eff} = \arcsin(\beta) \quad \Rightarrow \quad l_{eff} = \frac{\arcsin(\beta)}{\tau_c} \sqrt{\frac{2\mathcal{G}_c E_r h_r}{1+\rho}} \tag{34}$$

If $\beta = 0.95$, one gets:

$$\lambda_{eff} = 1.26 \quad \Rightarrow \quad l_{eff} = \frac{1.26}{\tau_c} \sqrt{\frac{2\mathcal{G}_c E_r h_r}{1+\rho}} \tag{35}$$

This value coincides (up to the factor $\sqrt{1+\rho}$) with the one provided by the Italian Standard CNR-DT200R1/13 (2013):

$$l_{eff} = \frac{1}{1.25\,\tau_c} \sqrt{\frac{\pi^2 \mathcal{G}_c E_r h_r}{2}} \tag{36}$$

which is actually based on the R-LSM herein described (and neglecting the deformability of the support, i.e. $\rho = 0$). Note that also the more recent Fib Bulletin 90/19 (International Federation for Structural Concrete, 2019) provides an effective bond length estimate based on the R-LSM solution (Eq. (33)).

Without entering details, it is worth noting that formulae provided by Standards other than CNR-DT200R1/13 and Fib Bulletin 90/19 are based on theoretical models coupled with empirical relationships. For instance, the Fib Bulletin 14/01 (International Federation for Structural Concrete, 2001) and the British TR55/2004 (Concrete Society, 2004) provide $l_{eff} = \sqrt{E_r h_r / 2 f_{ctm}}$, while the JCI 2003 (Japanese Concrete Institute, 2003) provides $l_{eff} = 0.125 (E_r h_r)^{0.57}$ (lengths must be expressed in millimeters, the other quantities in MPa and f_{ctm} is the average concrete tensile strength). In absence of suitable experimental values, also CNR-DT200R1/13 and Fib Bulletin 90/19 provide empirical relationships correlating $\mathcal{G}_c$ and τ_c with concrete tensile and compressive strength. CNR-DT200R1/13 have proved to be among the most accurate available Standards. For a detailed discussion about Standard performances, see Monaldo et al. (2019).

2.4. CCM: Rigid-Exponential Softening Model (R-ESM)

Strain gauges applied to the FRP plate provide the normal stresses in the reinforcement. Their spatial derivative provides the shearing interfacial stresses (Eq. (5)), from which the bond-slip law can be achieved experimentally. It is seen that, in some cases, a more realistic description of the softening

branch may be obtained assuming an exponential tail instead of a linear one. Assuming as before an infinite interface (elastic) stiffness prior to damage initiation, the bond-slip law now reads:

$$\tau(s) = \tau_c \exp(-2\, s/s_f) \tag{37}$$

where s_f is given by Eq. (20). Note that in the present case s_f is just a reference value without a precise mechanical meaning since there is no "final" displacement for an exponential softening: its value is just such that the underlying area is $\mathcal{G}_c$. Using normalized quantities, Eq. (37) reads:

$$\tilde{\tau}(\tilde{s}) = \exp(-2\tilde{s}) \tag{38}$$

and is plotted in Fig. 3a. As the R-LSM, also the R-ESM is a two-parameter model and it yields the maximum transferable load when all the bond length is in the softening regime. Upon substitution of Eq. (38) into Eq. (23), the differential problem now reads:

$$\begin{cases} \tilde{s}'' - \mathrm{e}^{-2\tilde{s}} = 0 \\ \tilde{s}(0) = 0 \\ \tilde{s}'(0) = 0 \end{cases} \tag{39}$$

with solution:

$$\tilde{s} = \ln\left[\cosh \xi\right] \tag{40}$$

$$\tilde{\tau} = \operatorname{sech}^2 \xi \tag{41}$$

$$\tilde{F}_c = \tilde{s}'(\lambda) = \int_0^{\lambda} \tilde{\tau}(\xi)\mathrm{d}\xi = \tanh \lambda \tag{42}$$

Eq. (42) is plotted in Fig. 3b: as expected, the debonding load provided by the linear softening model is higher than the one provided by the exponential softening model. For what concerns the effective length, setting $\tilde{F}_c = \beta$ into Eq. (42), yields:

$$\lambda_{eff} = \operatorname{arctanh}(\beta) \;\Rightarrow\; l_{eff} = \frac{\operatorname{arctanh}(\beta)}{\tau_c}\sqrt{\frac{2\mathcal{G}_c E_r h_r}{1+\rho}} \tag{43}$$

If $\beta = 0.95$, we get:

$$\lambda_{eff} = 1.83 \;\Rightarrow\; l_{eff} = \frac{1.83}{\tau_c}\sqrt{\frac{2\mathcal{G}_c E_r h_r}{1+\rho}} \tag{44}$$

Note that Eqs. (43-44) have the same numerical coefficient of Eqs. (17-18) but different dimensional expressions. On the other hand, Eqs. (43-44) have the same dimensional part of Eqs. (34-35) but a different numerical coefficient. More in detail, for $\beta = 0.95$ the estimate provided by the R-LSM (i.e. the one prescribed in Italian Standards) is about 2/3 of the one provided by the R-ESM.

2.5. Equivalent-LEBIM (Eq.-LEBIM)

While the previous two models can be directly compared, being based on the same quantities ($\mathcal{G}_c$ and τ_c) a comparison with LEBIM model (based on $\mathcal{G}_c$ and k) is possible only by introducing a (dimensionless) parameter linking the three quantities, cf. Cornetti et al (2012):

$$\mu = \frac{2k\mathcal{G}_c}{\tau_c^2} \tag{45}$$

The parameter μ is always greater than or equal to unity, $\mu \geq 1$. Typical values of μ for FRP-concrete interfaces are from a few units up to a few tens. By Eq. (45) and exploiting the normalization (22), Eq. (16) and (17) read:

$$\tilde{F}_c = \tanh\left(\lambda\sqrt{\mu}\right) \tag{46}$$

$$\lambda_{eff} = \operatorname{arctanh}(\beta)/\sqrt{\mu} \tag{47}$$

Eqs. (46) Eq. (47) clearly show that, with respect to the R-ESM (see Eqs. (42) and (43)), LEBIM model overestimates the debonding load (especially for small overlap lengths) and underestimates the effective bond length (see Fig. 3b): hence, the higher μ is, the larger the discrepancies between the LEBIM and extrinsic CCMs. Since LEBIM fails in catching the small bond length asymptote (i.e. the strength governed failure, Eq. (31)), extrinsic CCMs are usually considered as more reliable than LEBIM.

Although, for the present geometry and under the simplifying assumptions, all the models can be handled analytically, LEBIM model is usually much easier to apply than CCMs. Hence, a useful idea is to modify properly the LEBIM in such a way that it provides failure load estimates close to the CCMs. This can be easily achieved replacing the effective elastic stiffness k (given by Eq. (13)) with a fictitious, lower one, k_f, given by (Carozzi et al., 2015):

$$k_f = \frac{\tau_c^2}{2G_c} \tag{48}$$

This approach is here named Equivalent-LEBIM (Eq.-LEBIM). In dimensionless form, the constitutive law of the interface now reads (see Fig. 3a):

$$\tilde{\tau}(\tilde{s}) = \begin{cases} \tilde{s}, & \text{for} \quad 0 \le \tilde{s} \le 1 \\ 0, & \text{for} \quad \tilde{s} > 1 \end{cases} \tag{49}$$

while the differential problem Eq. (23) becomes:

$$\begin{cases} \tilde{s}'' - \tilde{s} = 0 \\ \tilde{s}'(0) = 0 \\ \tilde{s}'(\lambda) = \tilde{F} \end{cases} \tag{50}$$

with solution:

$$\tilde{s}(\xi) = \tilde{\tau}(\xi) = \frac{\tilde{F}}{\sinh(\lambda)} \cosh(\xi) \tag{51}$$

The maximum shear stress is achieved at the loaded end:

$$\tilde{\tau}_{max} = \tilde{\tau}(\lambda) = \frac{\tilde{F}}{\tanh(\lambda)} \tag{52}$$

Delamination occurs when $\mathcal{G}$ reaches $\mathcal{G}_c$, or - now it is equivalent - when the maximum shear stress reaches τ_c, i.e. $\tilde{\tau}(\lambda) = 1$. Correspondingly, the failure load is (Fig. 3b):

$$\tilde{F}_c = \tanh(\lambda) \tag{53}$$

an estimate which is close to Eq. (30) and coincident with Eq. (42). From Eq. (53) it follows that, according to Eq.-LEBIM, the effective length is also given by Eqs. (43-44).

At incipient failure, the stress field is obtained replacing Eq. (53) into Eq. (51). Thus:

$$\tilde{\tau}(\xi) = \frac{\cosh(\xi)}{\cosh(\lambda)} \tag{54}$$

Stress fields according to the models herein developed are compared in Fig. 4, where Eq. (54) is plotted together with Eqs. (15), (29) and (41) for two different bond lengths (λ= 1, 2, i.e. one smaller and one larger than $\pi/2$). Of course, in order to compare the (original) LEBIM model with the other models, the value for μ must be fixed (in the Fig. 4 we considered μ = 4).

The failure load predictions vs. bond length are compared in Fig. 3b, where Eq. (53) is plotted together Eqs. (30), (42) and (46). Coincidence between the debonding load prediction by Eq.-LEBIM and rigid-exponential softening interface models (i.e. Eqs. (53) and (42)) is rather surprising, even because the stress distributions at incipient delamination strongly differ as clearly shown in Fig. 4. Actually, the stresses are all in the elastic regime according to Eq.-LEBIM model, whereas the whole bond length is in the softening one according to the R-ESM. Nevertheless, the area beneath the two curves, i.e. the failure load, is the same in both models for any bond length.

It is evident that the introduction of a fictitious stiffness causes Eq.-LEBIM to fail when looking at the elastic compliance of the system (which turns out to be overestimated), but Eq.-LEBIM debonding load predictions agree or coincide with the ones provided by extrinsic CCMs. Moreover, in the following, we will show that failure load estimates provided by intrinsic CCMs and by FFM are close as well, so that Eq.-LEBIM turns out to be a very easy yet powerful tool to get rather accurate results.

A final comment about Eq.-LEBIM is its analogy with Equivalent-LEFM (Bažant & Planas, 1998). In fact, LEBIM represents LEFM applied to elastic interfaces; as such, it needs only elastic parameters and fracture energy, that is, it is not affected by the (interfacial) strength. The trick to replace the effective stiffness by the fictitious one (Eq. 48) is a way to take the interface strength into account and, hence, getting accurate predictions even for relatively low bond lengths. The trick works (for delamination along interfaces) in a way very similar to the one exploited by the so-called Equivalent-LEFM for homogeneous cracked bodies. Equivalent-LEFM requires to apply LEFM once an a-long crack has been replaced by a fictitious crack of (increased) length $a + (1/\pi) \times (K_{Ic}/\sigma_c)^2$, K_{Ic} and σ_c being the material fracture toughness and tensile strength, respectively. Modifying the geometry (and increasing its compliance), Equivalent-LEFM yields reliable (and close to CCM/FFM) predictions of failure loads even for short cracks; analogously, Eq.-LEBIM, by modifying the interface elastic stiffness, provides reliable (and close to CCM/FFM predictions) delamination loads even for relatively low bond lengths.

Finally, notice that an approach similar to the present one for mixed mode interface fracture can be found in Panagiotopoulos et al. (2018).

2.6. Finite Fracture Mechanics (FFM)

In order to take the strength, the fracture energy and the (actual) stiffness of the interface simultaneously into account, more complex models must be considered. They are *three-parameter* models. The first three-parameter model we introduce is based on Finite Fracture Mechanics (FFM, Cornetti et al. 2012).

FFM is a fracture criterion based on the assumption of a discrete crack growth. Fracture is supposed to occur whenever the available energy is larger than the energy needed to create the new crack surface and, simultaneously, the stress (or a function of the stress) acting on the region where crack will take place exceeds the interface strength. The former condition is the energy balance in discrete form (instead of Griffith's infinitesimal one characterizing LEFM); the latter is a stress requirement and can be chosen according to the problem at hand. The interface behaviour is supposed to be linear elastic prior to damage onset, with stiffness k ($\tau = k\, s$), i.e. μ in the dimensionless form ($\tilde{\tau} = \mu\, \tilde{s}$), see Fig. 5a.

Denoting by Δ the length of the finite crack increment, the discrete energy balance requires that:

$$\int_0^{\Delta} \mathcal{G}(a)\, \mathrm{d}a \geq \mathcal{G}_c\, \Delta \tag{55}$$

a being the length of the debonding; as a varies from 0 to Δ, the actual bond length l' varies from l to $l-\Delta$. Since, as already observed, $\mathcal{G} = \tau_{max}^2 / 2k$, Eq. (55) becomes:

$$\int_{l-\Delta}^{l} \tau_{max}^2(l')\, \mathrm{d}l' \geq 2k\mathcal{G}_c\, \Delta \tag{56}$$

A typical choice for the stress condition is requiring that, over the crack increment, the stress exceeds the strength at any point (Leguillon, 2002). However, for short overlap lengths, this choice yields failure loads higher than the interface strength times the bonded area. This odd feature seems not to be confirmed by experiments and, hence, it will be left out. A second possibility is requiring that the average stress over the finite crack step exceeds the interface strength (Cornetti et al., 2006).

$$\int_{l-\Delta}^{l} \tau(x)\, \mathrm{d}x \geq \tau_c\, \Delta \tag{57}$$

Using the normalized quantities (22) and introducing the dimensionless crack step $\delta = \Delta / l_{ch}$, Eqs. (56) and (57) read:

$$\begin{cases} \int_{\lambda-\delta}^{\lambda} \tilde{\tau}_{max}^2(\lambda')\,d\lambda' \geq \mu\,\delta \\ \int_{\lambda-\delta}^{\lambda} \tilde{\tau}(\xi)\,d\xi \geq \delta \end{cases} \tag{58}$$

According to FFM, the failure load is the minimum one satisfying these two inequalities. The present geometry is a so-called positive geometry, since the crack driving force $\mathcal{G}$ increases during crack growth while the stress decreases moving away from the debonding crack tip. Accordingly, the failure load is achieved when the two inequalities are strictly fulfilled, and Eq. (58) reverts to a system of two equations in two unknowns: the critical load and the crack advancement.
In dimensionless form, Eq. (15) reads:

$$\tilde{\tau}(\xi) = \sqrt{\mu}\,\frac{\cosh(\xi\sqrt{\mu})}{\sinh(\lambda\sqrt{\mu})}\,\tilde{F} \tag{59}$$

Hence:

$$\tilde{\tau}_{max}(\lambda') = \sqrt{\mu}\,\coth(\lambda'\sqrt{\mu})\,\tilde{F} \tag{60}$$

Upon substitution of Eqs. (59-60) into (58) and upon integration, one can equate the failure loads from both the system equations, so that the following equation in the crack advance unique unknown δ is achieved:

$$\delta\sinh^2(\lambda\sqrt{\mu})\left\{\delta\sqrt{\mu} - \coth(\lambda\sqrt{\mu}) + \coth\left[(\lambda-\delta)\sqrt{\mu}\right]\right\} = \sqrt{\mu}\left\{\sinh(\lambda\sqrt{\mu}) - \sinh\left[(\lambda-\delta)\sqrt{\mu}\right]\right\}^2 \tag{61}$$

Eq. (61) can be easily solved numerically, looking for solutions within the range $0 < \delta < \lambda$. Once the value δ is found, we can obtain the failure load either from the first or the second equation of the system (58). Choosing the second one, we get:

$$\tilde{F}_c = \frac{\delta\sinh(\lambda\sqrt{\mu})}{\sinh(\lambda\sqrt{\mu}) - \sinh\left[(\lambda-\delta)\sqrt{\mu}\right]} \tag{62}$$

Since FFM depends on three parameters, the dimensionless debonding load depends not only on λ (as for the previous models) but also on μ. Plots of the debonding load vs. bond length are given in Fig. 5b for different μ values: load increases as μ increases. For $\mu = 1$ (elastic-perfectly brittle interface) FFM reverts to Eq.-LEBIM and, hence, the failure load is given by Eq. (53). For $\mu \to \infty$ the curve tends to the bilinear line given by Eqs. (31) and (32). This last case (i.e. $\mu \to \infty$) can be regarded as the Rigid-FFM solution (Mirzaei et al., 2021) and, moreover, coincides with the solution provided by the Dugdale model (not addressed in the present manuscript).

Before proceeding, it is worth observing the different influence of the three interface parameters ($\mathcal{G}_c$, τ_c and k) on the debonding load. The fracture energy $\mathcal{G}_c$ has the strongest influence, defining the range $(0, F_c^{\infty})$ of admissible values (F_c^{∞} depends only on $\mathcal{G}_c$, see Eq. (3)). A weaker, yet significant, influence is given by the interfacial strength τ_c, since, for a given $\mathcal{G}_c$, λ is proportional to τ_c through l_{ch} (Eq. (21)). Finally, the elastic stiffness k does not affect either F_c^{∞} or l_{ch}; k affects the solution only through the parameter μ (Eq. (45)). Thus, its influence on the failure load is definitely weaker. For a given couple of $\mathcal{G}_c$ and τ_c values, the failure load increases as k (i.e. μ) increases (see Fig. 5b). However, for a given λ value, the relative difference between failure load predictions is always less than 31% for any μ value (with respect to the lower value).

Although the effect of the stiffness k is relatively small on the failure load, its effect on the effective bond length is much higher because of the shape of the load vs. bond length curves. As evident in Fig. 5b, the effective length decreases as k (i.e. μ) increases. With the aim to determine

analytically the effective length λ_{eff}, we simply observe that Eqs. (61) and (62) must hold along with $\tilde{F}_c = \beta$. It means that λ_{eff} is given by the solution of the following system (in λ_{eff} and δ):

$$\begin{cases} \beta^2 \left\{ \coth\left[(\lambda_{eff} - \delta)\sqrt{\mu} \right] - \coth\left(\lambda_{eff} \sqrt{\mu} \right) \right\} = \left(1 - \beta^2 \right) \delta \sqrt{\mu} \\ \beta \left\{ \sinh(\lambda_{eff} \sqrt{\mu}) - \sinh\left[(\lambda_{eff} - \delta)\sqrt{\mu} \right] \right\} = \delta \sinh(\lambda_{eff} \sqrt{\mu}) \end{cases} \tag{63}$$

Solution to (63) is easily achieved numerically: λ_{eff} varies from β for $\mu \to \infty$ to arctanh(β) for μ = 1, i.e. from 0.95 to 1.83 if β = 0.95. Thus, its maximum value is about twice the minimum one.

2.7. CCM: Linear Elastic-Linear Softening Model (LE-LSM)

In the second three-parameter model considered the interface behaviour is described by a linear elastic-linear softening cohesive law:

$$\tau(s) = \begin{cases} k\, s, & \text{for} \quad 0 \le s \le s_c \\ \tau_c \dfrac{s_f - s}{s_f - s_c}, & \text{for} \quad s_c < s \le s_f \\ 0, & \text{for} \quad s > s_f \end{cases} \tag{64}$$

where $s_c = \tau_c / k$ is the relative displacement at the peak stress τ_c and, as before, the final displacement s_f is given by Eq. (20). In dimensionless form, Eq. (64) reads:

$$\tilde{\tau}(\tilde{s}) = \begin{cases} \mu\, \tilde{s}, & \text{for} \quad 0 \le \tilde{s} \le 1/\mu \\ \dfrac{\mu}{\mu - 1}(1 - \tilde{s}), & \text{for} \quad 1/\mu < \tilde{s} \le 1 \\ 0, & \text{for} \quad \tilde{s} > 1 \end{cases} \tag{65}$$

Note that, for the LE-LSM, the parameter μ (Eq. (45)) is also equal to the ratio of the final relative displacement to the peak one, i.e. $\mu = s_f / s_c$. The linear elastic-linear softening cohesive law is plotted in Fig. 6a for different values of the parameter μ. It is evident that the present model spans from the Eq.-LEBIM for μ = 1 up to the R-LSM as $\mu \to \infty$.

The solution of the differential equation (23) along with the bond-slip law (65) is not trivial: the debonding process has to be subdivided in different stages: moreover, there are two different solutions, one for short and one for long overlap lengths (for details see, e.g, Carpinteri & Cornetti (2011) and Caggiano et al. (2012)). However, as far as we are interested only in the maximum (i.e. the failure) load, there is no need to distinguish between long and short bond joints, since the maximum load is achieved in the elastic-softening stage when the two solutions are still coincident.

Let us mark by a_p the length of the process (i.e. softening) zone at the loaded end when the load is maximum and by α_p its normalized counterpart, i.e. $\alpha_p = a_p / l_{ch}$. Without going into details, α_p is given by the solution of the following transcendental equation (Yuan et al., 2004):

$$\sqrt{\mu - 1}\, \tanh\left[\sqrt{\mu} \left(\lambda - \alpha_p \right) \right] = \tan\left(\alpha_p \sqrt{\frac{\mu}{\mu - 1}} \right) \tag{66}$$

The maximum is then achieved upon substitution of the solution of Eq. (66) into the following expression:

$$\tilde{F}_c = \sqrt{\frac{\mu}{\mu - 1}}\, \sin\left(\alpha_p \sqrt{\frac{\mu}{\mu - 1}} \right) \tag{67}$$

The value of the failure load vs. the bond length is plotted in Fig. 6b for different values of the parameter μ. As expected, the solution ranges from the Eq.-LEBIM for μ = 1 up to the R-LSM as $\mu \to \infty$. The same considerations about the effect of the interface parameters provided for the FFM model hold also in the present case: the effect of k is now even smaller (always below 12%).

Comparison between Figs. 5b and 6b shows the good agreement between the FFM approach and the LE-LSM model; an agreement that becomes excellent for low μ values (about $\mu < 5$). Note that usually FFM is much easier to apply than elastic-softening CCMs: even in the present case, where the CCM solution is semi-analytical, we skipped the derivation, because too long, and provided directly the results. Thus, the agreement between FFM and CCM clearly indicates FFM as an excellent candidate model to achieve fast yet accurate results.

With the aim of determining the effective bond length according to the LE-LSM, we have simply to set $\tilde{F}_c = \beta$ in Eq. (67). By Eq. (66) and some analytical manipulation, we get the following closed-form expression for the effective length:

$$\lambda_{eff} = \sqrt{\frac{\mu-1}{\mu}}\ \arcsin\left(\beta\sqrt{\frac{\mu-1}{\mu}}\right) + \frac{1}{\sqrt{\mu}}\operatorname{arctanh}\frac{\beta}{\sqrt{\beta^2+\left(1-\beta^2\right)\mu}} \tag{68}$$

It varies from $\arcsin(\beta)$ for $\mu \to \infty$ up to $\operatorname{arctanh}(\beta)$ for $\mu = 1$ (i.e. from 1.26 up to 1.83 if $\beta = 0.95$). Thus, also according to the LE-LSM, the relative difference between extreme λ_{eff} values can be rather high (i.e. up to about 45%).

2.8. CCM: Linear Elastic-Exponential Softening Model (LE-ESM)

In the last (three-parameter) model considered the interface behaviour is described by a linear elastic-exponential softening cohesive law. Accordingly, the bond-slip law reads:

$$\tau(s) = \begin{cases} k\, s, & \text{for} \quad 0 \le s \le s_c \\ \tau_c \exp\left(-2\dfrac{s-s_c}{s_f-s_c}\right), & \text{for} \quad s > s_c \end{cases} \tag{69}$$

where s_f is always given by Eq. (20). The cohesive law (69) can be cast in dimensionless form as:

$$\tilde{\tau}(\tilde{s}) = \begin{cases} \mu\, \tilde{s}, & \text{for} \quad 0 \le \tilde{s} \le 1/\mu \\ \exp\left(-2\dfrac{\mu\, \tilde{s}-1}{\mu-1}\right), & \text{for} \quad \tilde{s} > 1/\mu \end{cases} \tag{70}$$

The linear elastic-exponential softening cohesive law is plotted in Fig. 7a for different values of the parameter μ. It is evident that the LE-ESM model spans from the Eq.-LEBIM for $\mu = 1$ up to the R-ESM model as $\mu \to \infty$.

The solution of the differential equation (23) along with the bond-slip law (70) can be found in Cornetti & Carpinteri (2011) in a fully analytical form. Expressions are somewhat more complex with respect to the linear elastic-linear softening case, but the advantage is that there is no distinction between short and long bond lengths. For what concerns the maximum transferable load, it is achieved in the elastic-softening stage. Without going into details, denoting as before by α_p the normalized process zone length at maximum load, the load is given by the following expression:

$$\tilde{F} = \gamma\sqrt{\frac{\mu-1}{\mu}}\ \tanh\left\{\gamma\ \alpha_p\sqrt{\frac{\mu}{\mu-1}} + \ln\left[\gamma + \frac{\tanh\left((\lambda-\alpha_p)\sqrt{\mu}\right)}{\sqrt{\mu-1}}\right]\right\} \tag{71}$$

with:

$$\gamma = \sqrt{1+\frac{\tanh^2\left[(\lambda-\alpha_p)\sqrt{\mu}\right]}{\mu-1}} \tag{72}$$

By letting α_p vary from 0 up to λ, the load first increases and then decreases. The debonding load $\tilde{F}_c$ is easily achieved by looking for the maximum numerically. Its value is plotted vs. the bond length in Fig. 7b for different values of the parameter μ. As expected, the solution ranges from the

Eq.-LEBIM for $\mu = 1$ up to the R-ESM as $\mu \to \infty$, which coincide. Thus, the failure load is almost insensitive to μ (i.e. to the elastic stiffness k): for a given λ, differences are always below 2%. It means that, for engineering purposes, the debonding load is always given by Eq. (42) (or equally by Eq. (53)) for any linear elastic-exponential softening law with the same fracture energy and interfacial strength, i.e. for any curve in Fig. 7a.

A slightly bit higher variation is found for the effective bond lengths, whose values have to be sought numerically by intersecting the curves in Fig. 7b with the horizontal line $\tilde{F}_c = \beta$. For any μ value, the (dimensionless) effective bond length λ_{eff} is comprised between 1.83 and 1.99.

3. Discussion and comparison with experimental data

Taking $\beta = 0.95$, in Fig. 8 we plotted the (dimensionless) effective bond length λ_{eff} vs. $1/\mu$ according to all the models considered in the previous section. Except LEBIM, two-parameter models are not influenced by the interface elastic stiffness (through μ). Elastic stiffness does affect three-parameter models; however, as evident in Fig. 8, only the LE-LSM and the FFM approach show a significant dependence on μ and, for not too rigid interfaces (i.e. μ values close to unity), they provide effective bond length estimates very close each other.

In absence of a clear indication about the interface elastic stiffness, from Fig. 8 it is reasonable to propose for the effective bond length the highest estimates among all the models provided herein, i.e.:

$$l_{eff} = \frac{2}{\tau_c}\sqrt{\frac{2\mathcal{G}_c E_r h_r}{1+\rho}} \tag{73}$$

Alternatively, one can propose Eq. (44), which is close to Eq. (73) and supported by two models among the ones herein provided (namely, the Eq.-LEBIM and the R-ESM). Moreover, Eq. (44) represents the upper bound also for the FFM and LE-LSM.

It must be stressed that estimates (73) and (44) are 59% and 45%, respectively, higher than the value prescribed by Eq. (36), whose uncritical use in Design Guidelines (i.e. if material behaviors other than the rigid-linear softening one rule the interface mechanics) must hence be regarded as potentially dangerous. On the other hand, a lower effective bond length can be assumed only if more information is available. That is, if the elastic interface stiffness is known with sufficiently high accuracy and the softening branch of the interface law is not too steep (i.e. not exponential), the analysis presented in the previous section suggests the use of an effective bond length value provided either by the FFM approach or the LE-LSM, i.e. Eqs. (63) and (68). In such a case, Eq. (73) turns out to be conservative.

To corroborate these conclusions, we finally provide some comparisons between the analytical results presented in Section 2 and experimental data taken from the Literature. In order to perform such a comparison, one needs to know the interface strength and fracture energy and, possibly, also the interface elastic stiffness. As outlined e.g. in Ali-Ahmad et al. (2006) or Ferracuti et al. (2007), the bond-slip law (and its parameters) can be extracted numerically by measuring the axial strain field in the FRP during a *single* test: in fact, the derivative of the strain is proportional to the interfacial shear stresses (Eq. (5)) and the integral of the strain is proportional to the slip. Of course, precise experimental measures are needed; moreover, a large scatter is usually met, since the "measured" interface law varies from point to point (of the interface).

Alternatively (see, e.g., Cottone & Giambanco, 2009; Franco & Royer-Carfagni, 2014) the interface parameters can be obtained by measuring the debonding loads for *several* specimens with different bond lengths. This approach has the great advantage to by-pass all the technical difficulties of a sophisticated experimental apparatus necessary to determine the interface constitutive law. Of

course, an experimental campaign with tests spanning from short to long bond lengths is needed. Approximately, this qualitative feature can be translated quantitatively by requiring that the ratio between maximum and minimum debonding load ($\max\{F_{c,i}\}/\min\{F_{c,i}\}$) and the ratio between maximum and minimum debonding load to bond length ratio ($\max\{F_{c,i}/l_i\}/\min\{F_{c,i}/l_i\}$) must be preferably larger than 2 (i is the generic test number in an experimental campaign conducted over $i = 1,\ldots,n$ tests).

We will follow this second way, thus selecting experimental data satisfying or being close to the above requirements. To make things even simpler, the short and long bond lengths asymptotes depend only on shear strength and fracture energy, respectively. Thus, by means of Eqs. (31) and (32), we can estimate the interface fracture energy and the interface strength by means of the following expressions:

$$\mathcal{G}_c = \frac{1+\rho}{2E_r h_r t_r^2} \max_{i=1,\ldots,n}{}^2 \left\{F_{c,i}\right\} \tag{74}$$

$$\tau_c = \frac{1}{t_r} \max_{i=1,\ldots,n} \left\{\frac{F_{c,i}}{l_i}\right\} \tag{75}$$

The first set of data we considered is by Mazzotti et al. (2008), second series, four tests in total. They performed single-lap shear tests over concrete blocks of cross sections $t_b \times h_b = 150$ mm $\times$ 200 mm. Cross section of the FRP lamina is $t_r \times h_r = 80$ mm $\times$ 1.2 mm. Young's moduli are $E_b = 30.7$ GPa and $E_r = 195.2$ GPa, for concrete and FRP, respectively. The bond lengths were equal to 50, 100, 200, 400 mm. Eqs. (74) and (75) provide the following estimates for interface fracture energy and shear strength: $\mathcal{G}_c = 0.47$ N/mm and $\tau_c = 5.5$ MPa. No information was given about the interface elastic compliance: thus, we limited the analytical-experimental comparison to two-parameter models. Based on the above values, we plotted in Fig. 9 the predictions by the rigid-softening models – Eq. (30) for the R-LSM and Eq. (42) for the R-ESM – along with the experimental data. It is evident that the R-ESM (or, the same, the Eq.-LEBIM) provides a good agreement with experimental data, better than the R-LSM. In the same figure, we plotted the effective length estimates Eqs. (35) and (44), respectively equal to 105 mm and 154 mm. For the few data available, it is evident that the highest one, related to exponential softening / equivalent LEBIM, performs better, although the failure load for the 200 mm bond length still falls beneath the 95% F_c^∞ line.

The second set of data are the ones by Carrara et al. (2011). In this paper the Authors were interested in a unloaded-end displacement-controlled test. Thus, they performed several tests although most of them relates to relatively short bond length. More precisely, the Authors performed single-lap shear tests over concrete blocks of cross sections $t_b \times h_b = 150$ mm $\times$ 90 mm. Cross section of the FRP lamina is, on average, $t_r \times h_r = 30$ mm $\times$ 1.3 mm. Young's moduli are $E_b = 28.7$ GPa and $E_r = 168.5$ GPa, for concrete and FRP, respectively. The bond lengths were equal to 30, 60, 90, 120, 150 mm. Eqs. (74) and (75) provide the following estimates for interface fracture energy and shear strength: $\mathcal{G}_c = 1.0$ N/mm and $\tau_c = 5.9$ MPa. Shear modulus of the adhesive was $G_a = 1.35$ GPa and the adhesive layer thickness was $h_a = 1.3$ mm. Using Eq. (41) with $h_{bi} = 20$mm, by Eq. (45) we obtained $\mu = 22$. Based on the above values, we plotted in Fig. 10 the predictions by the R-LSM and the R-ESM along with the experimental data; here we were forced to use dimensionless plot since the FRP width is slightly changing from one specimen to another. It is evident that also in this case the R-ESM (coinciding with the Eq.-LEBIM) provides a good agreement with the experimental data, better than the R-LSM. We conclude that the softening exponential model is the best one for Carrara et al.'s data. Since for the LE-ESM the effect of μ is almost negligible, we didn't take it into account. In Fig. 10 we plotted also the effective length estimates Eqs. (35) and (44), respectively equal to 140 mm and 206 mm. The lowest estimate fails in one case (a test with the highest length - $l = 150$ mm, higher than l_{eff} - have debonding loads lower than 95% F_c^∞); the higher estimate

presents two cases with the highest length (l = 150 mm, now lower than l_{eff}) showing a debonding load higher than 95% F_c^{∞}. Thus, safety arguments suggest the use of Eq. (44) instead of Eq. (35) also in this case.

The third and fourth set are the third and fourth series of an experimental campaign by Dai et al. (2006). The Authors did not provide any information about the geometry of the concrete block; thus we decided to consider it as rigid (i.e. $\rho = 0$). The width of the FRP lamina is t_r = 50 mm. For what concerns the third series, the product of the FRP Young's modulus time its thickness is $E_r \times t_r$ = 75900 N/mm while the bond lengths are equal to 20, 40, 80, 150, 300 mm. Eqs. (74) and (75) provide the following estimates for interface fracture energy and shear strength: $\mathcal{G}_c$ = 0.69 N/mm and τ_c = 5.6 MPa. The concrete shear modulus is G_b = 13500 MPa; the ratio between the shear modulus of the adhesive and its thickness is G_a / h_a =1140 N/mm^3. Using Eq. (41) with h_{bi} = 20 mm, we obtain an interfacial shear stiffness equal to k = 424 N/mm^3 yielding, by Eq. (45), μ = 18.7. Based on the above values, we plot in Fig. 11 the predictions by the rigid-softening models along with the experimental data. In this case, the R-LSM performs better. Wishing to take the interface stiffness into account (through μ), we can apply the three-parameter models, namely the LE-LSM and the FFM models. It is evident that they both provide an excellent fitting of the experimental data. In Fig. 11 we plotted also the effective length estimates Eqs. (35) and (44), respectively equal to 72 mm and 106 mm. As expected, in this case Eq. (35) performs better, the latter being too conservative. Also the three-parameter models, through Eqs. (63) and (68), provide excellent estimates of the effective length, 66 mm and 75 mm respectively, plotted in Fig. 11 as well.

The comparison with the experimental results of the fourth series tested by Dai et al. (2006) is plotted in Fig. 12. For what concerns their series 4, the product of the FRP Young's modulus time its thickness is $E_r \times t_r$ = 50600 N/mm while the bond lengths are equal to 20, 40, 60, 200 mm, respectively. Eqs. (74) and (75) provide the following estimates for interface fracture energy and shear strength: $\mathcal{G}_c$ = 0.82 N/mm and τ_c = 4.6 MPa. As in the series 3, the interfacial shear stiffness is k = 424 N/mm^3, yielding now, by Eq. (45), μ = 33.3. Based on the above values, we plot in Fig. 12 the predictions by the rigid-softening models along with the experimental data. Also in this case, the R-LSM performs better. By exploiting the computed μ value, we plot also the LE-LSM and the FFM models. They both interpret well the experimental data, FFM providing the best fitting. In Fig. 12 we draw also the effective length estimates Eqs. (35) and (44), respectively equal to 79 mm and 115 mm. As expected, in this case Eq. (35) performs better, the latter being too conservative. Also the three-parameter models, through Eqs (63) and (68), provide excellent estimates of the effective length, 68 mm and 81 mm respectively, plotted in Fig. 12 as well.

Finally, in Fig. 13 we plot all the experimental data considered separately up to now in a unique, dimensionless plot. The horizontal line represents the 95% value of the maximum transferable load. The vertical lines represents the effective bond length estimates based on the R-LSM (Eq. 35), currently used by the Italian Standards, and on the LE-ESM (Eq. 73). As already observed, the latter one is 59% higher than the former one and, thus, more conservative. Both expressions are simple and relatively easy to be determined, needing only the interface strength and fracture energy, i.e. they do not depend on the interface stiffness. However, differently from Eq. (35), Eq. (73) represents the upper bound for all the models considered in the previous Section, for any interface stiffness.

The best effective length estimate would be the one dividing, together with the 95% maximum load line, the load vs. bond length plane in four quadrants such that the experimental data all fall in the first (safe values) and in the third (unsafe values) quadrants. It is apparent that, because of simplifying assumptions, experimental scattering, etc. such an estimate does not exist within the framework here outlined. However, both the estimates (35) and (73) work pretty well: Eq. (35) lets out only one datum in the second quadrant (false unsafe) and two in the fourth (false safe), see Fig. 13a; Eq. (73) lets out four data in the second quadrant (false unsafe) and just one in the fourth (false safe), see Fig. 13b. Of course, the major problem is represented by false safe cases and, thus, use of Eq. (73) is recommended.

4. Conclusions

In the present paper, we reviewed eight analytical models able to describe the single-lap shear test, and compared synoptically the results. More in detail, we analysed Linear Elastic Fracture Mechanics, Linear Elastic Brittle Interface Model, Finite Fracture Mechanics, Extrinsic and Intrinsic Cohesive Softening models. The common denominator is that they are all one-dimensional shear lag models and, thus, sufficiently easy to be handled analytically. Models are classified as one-, two-, three-parameter models as long as the interface is characterized by one, two or three parameters among fracture energy, tensile strength, elastic stiffness.
Main conclusions are as follows:

- Among the three parameters characterizing the interface bond-slip law, the fracture energy is the one that has the strongest influence on the mechanical response of the single-lap shear test. A smaller yet significant influence is given by the interfacial strength, while the interfacial elastic stiffness usually provides the smallest effect.
- To catch the increment of the debonding load due to increasing bond length, at least two-parameter interface models are needed. Proper dimensionless formulation allows one to get a unique curve (two-parameter models) or a family of curves (three-parameter models) providing the debonding load vs. bond length.
- Two-parameter models: the shape of the bond-slip law significantly affect the value of effective bond length. Equivalent-LEBIM and Rigid-Exponential Softening Model provide the same effective bond length estimate. Rigid-Linear Softening Model provide a lower estimate.
- Design codes are mostly based on Rigid-Linear Softening Model. Thus, their uncritical use may lead to un-conservative (low) effective bond length estimates.
- Three-parameter models: the effect of the elastic stiffness on the load vs. bond length curves is almost negligible for the Linear Elastic-Exponential Softening Model, whereas it is significant according to the Finite Fracture Mechanics model and to the Linear Elastic-Linear Softening Model.
- An effective bond length formula based on interface strength and fracture energy (i.e., independent from elastic stiffness) has been set forward. The formula is un upper bound of the estimates provided by all the reviewed models, and it is thought to be useful for safe design rules.
- Comparison between the reviewed models and four datasets from the Literature has been provided. It was not possible to assess which is the best one since models performed differently according to different datasets. However, the proposed effective bond length formula performed satisfactorily.

Acknowledgements: The research was supported by the Spanish Ministry of Science, Innovation and Universities and European Regional Development Fund (Project PGC2018-099197-B-I00) and Consejería de Economía y Conocimiento de la Junta de Andalucía and Programa Operativo FEDER Andalucía 2014–2020 (Projects US-1266016 and P18-FR-1928).

References

Ali-Ahmad M., Subramaniam K., Ghosn M. (2006) *Experimental investigation and fracture analysis of debonding between concrete and FRP sheets*. Journal of Engineering Mechanics, 132:914-923.

Alfano G. (2006) On the influence of the shape of the interface law on the application of cohesive-zone models. Composites Science and Technology 66: 723-730.

Ascione F., Mancusi G. (2010) *Failure Criteria for FRP Adhesive Lap Joints: A Comparative Analysis*. Mechanics of Advanced Materials and Structures, 17:157-164.

Bažant Z.P., Planas J. (1998) *Fracture and Size Effect in Concrete and Other Quasibrittle Materials*. CRC Press, Boca Raton.

Bennati S., Colleluori M., Corigliano D., Valvo P.S. (2009) *An enhanced beam-theory model of the asymmetric double cantilever beam (ADCB) test for composite laminates*. Composite Science and Technology 69:1735–1745.

Biscaia H.C., Borba I.S., Silva C., Chastre C. (2016) *A nonlinear analytical model to predict the full-range debonding process of FRP-to-parent material interfaces free of any mechanical anchorage devices*. Composite Structures 138:52-63.

Biscaia H.C., Chastre C., Silva M.A.G. (2017) *Analytical model with uncoupled adhesion laws for the bond failure prediction of curved FRP-concrete joints subjected to temperature*. Theoretical and Applied Fracture Mechanics 89:63-78.

Bocciarelli M. (2021) *A new cohesive law for the simulation of crack propagation under cyclic loading. Application to steel- and concrete-FRP bonded interface*. Theoretical and Applied Fracture Mechanics 114: 102992.

Caggiano A., Martinelli E., Faella C. (2012). *A fully-analytical approach for modelling the response of FRP plates bonded to a brittle substrate.* International Journal of Solids and Structures 49:2291-2300.

Carozzi F.G., Colombi P., Poggi C. (2015) *Calibration of end-debonding strength model for FRP-reinforced masonry.* Composite Structures 120:366-377.

Carrara P., Ferretti D., Freddi F., Rosati G. (2011) *Shear tests of carbon fiber plates bonded to concrete with control of snap-back*. Engineering Fracture Mechanics 78:2663-2678.

Chen J.F., Teng, J.G. (2001) *Anchorage strength models for FRP and steel plates bonded to concrete.* Journal of Structural Engineering 127:784-791.

CNR-DT 200 R1/2013 (2013) *Istruzioni per la Progettazione, l'Esecuzione ed il Controllo di Interventi di Consolidamento Statico mediante l'utilizzo di Compositi Fibrorinforzati*. Consiglio Nazionale delle Ricerche, Rome, Italy.

Concrete Society (2004) *Design Guidance for Strengthening Concrete Structures Using Fibre Composite Materials*. Technical Report 55, 2nd edition, Camberley, UK.

Cornetti P., Carpinteri A. (2011) *Modelling the FRP-concrete delamination by means of an exponential softening law*. Engineering Structures 33:1988-2001.

Cornetti P., Mantič V., Carpinteri A. (2012) *Finite fracture mechanics at elastic interfaces*. International Journal of Solids and Structures 49:1022-1032.

Cornetti P., Pugno N., Carpinteri A., Taylor D. (2006) *Finite fracture mechanics: a coupled stress and energy failure criterion*. Engineering Fracture Mechanics 73:2021-2033.

Cottone A., Giambanco G. (2009) *Minimum bond length and size effects in FRP–substrate bonded joints*. Engineering Fracture Mechanics 76:1957-1976.

Dai J., Ueda T., Sato Y. (2006) *Unified analytical approaches for determining shear bond characteristics of FRP-concrete interfaces through pullout tests*. Journal of Advanced Concrete Technology 4:133-145.

D'Antino T., Pellegrino C. (2014) *Bond between FRP composites and concrete: Assessment of design procedures and analytical models*. Composites Part B: Engineering 60:440-456.

De Maio U., Greco F., Leonetti L., Nevone Blasi P., Pranno A. (2022) *An investigation about debonding mechanisms in FRP-strengthened RC structural elements by using a cohesive/volumetric modeling technique*. Theoretical and Applied Fracture Mechanics 117, 103199.

De Lorenzis L., Miller B., Nanni A. (2001) *Bond of fiber-reinforced polymer laminates to concrete* ACI Materials Journal 98:256-264.

De Lorenzis L., Zavarise G. (2009) *Cohesive zone modeling of interfacial stresses in plated beams.* International Journal of Solids and Structures 46:4181-4191.
De Lorenzis L., Zavarise G. (2010) *Debonding analysis of thin plates from curved substrates*. Engineering Fracture Mechanics 77:3310-3328.
Ferracuti B., Savoia M., Mazzotti C. (2007) *Interface law for FRP–concrete delamination*. Composite Structures 80:523-531.
Franco A., Royer-Carfagni G. (2014) *Effective bond length of FRP stiffeners*. International Journal of Non-Linear Mechanics 66:126-138.
Grande E., Imbimbo M., Marfia S., Sacco E. (2019) *Numerical simulation of the de-bonding phenomenon of FRCM strengthening systems*. Frattura ed Integrità Strutturale 13:321-333.
He L., Wu Y.F., Xiao Y. (2015) *Analytical solution for externally bonded joints considering snap-back*. Journal of Composites for Construction 19 (5), art. no. 04014077.
International Federation for Structural Concrete (2001) fib Bulletin No. 14: *Externally bonded FRP reinforcement for RC structures*, Technical Report, Lausanne, Switzerland.
International Federation for Structural Concrete (2019) fib Bulletin No. 90: *Externally applied FRP reinforcement for concrete structures*, Technical Report, Lausanne, Switzerland.
Japan Concrete Institute (2003) *Technical report of technical committee on retrofit technology*. Proc. Int. Symp. on Latest Achievement of Technology and Research on Retrofitting Concrete Structures, Japan Concrete Institute (JCI), Tokyo, Japan.
Krenk S. (1992) *Energy release rate of symmetric adhesive joints*. Engineering Fracture Mechanics 43:549-559.
Leguillon D. (2002) *Strength or toughness? A criterion for crack onset at a notch.* European Journal of Mechanics A/Solids 21:61-72.
Lenci S. (2001) *Analysis of a crack at a weak interface*. International Journal of Fracture 108:275-290.
Leung C.K.Y., Yang Y. (2006) *Energy-based modelling approach for debonding of FRP plate from concrete substrate*. Journal of Engineering Mechanics-ASCE 132:583-593.
Lu X.Z., Teng J.G., Ye L.P., Jiang J.J. (2005) *Bond–slip models for FRP sheets/plates bonded to concrete*. Engineering Structures 27:920-937.
Malena M., Focacci F., Carloni C., de Felice G. (2017) *The effect of the shape of the cohesive material law on the stress transfer at the FRP-masonry interface*. Composites Part B: Engineering 110:368-380.
Malena M. (2018) *Closed-form solution to the debonding of mortar based composites on curved substrates*. Composites Part B: Engineering 139:249-258,
Mantič V., Távara L., Blázquez A., Graciani E., París F. (2015) *A linear elastic-brittle interface model: application for the onset and propagation of a fibre-matrix interface crack under biaxial transverse loads*. International Journal of Fracture 195:15–38.
Martinelli E. (2021) *Closed-Form Solution Procedure for Simulating Debonding in FRP Strips Glued to a Generic Substrate Material*. Fibers 9, 22.
Martinelli E., Caggiano A. (2021) *Low-Cycle Fatigue of FRP Strips Glued to a Quasi-Brittle Material.* Materials 14, 7753.
Mazzotti C., Savoia M., Ferracuti B. (2008) *An experimental study on delamination of FRP plates bonded to concrete*. Construction and Building Materials 22:1409-1421.
Mirzaei A.M., Corrado M., Sapora A., Cornetti P. (2021) *Analytical modeling of debonding mechanism for long and short bond lengths in direct shear tests accounting for residual strength*. Materials 14, 6690.
Monaldo E., Nerilli F., Vairo G. (2019) *Effectiveness of some technical standards for debonding analysis in FRP-concrete systems*. Composites Part B: Engineering 160:254-267.
Muñoz-Reja M., Cornetti P., Távara L., Mantič V. (2020a) *Interface crack model using finite fracture mechanics applied to the double pull-push shear test*. International Journal of Solids and Structures 188-189:56-73.

Muñoz-Reja M., Távara L., Mantič V., Cornetti P. (2020b) *A numerical implementation of the Coupled Criterion of Finite Fracture Mechanics for elastic interfaces*. Theoretical and Applied Fracture Mechanics 108, 102607.

Panagiotopoulos C.G., Mantič V., Roubíček T. (2018) *Two adhesive-contact models for quasistatic mixed-mode delamination problems*. Mathematics and Computers in Simulation, 145:18-33.

Rabinovitch O. (2008) *Debonding analysis of fiber-reinforced-polymer strengthened beams: Cohesive zone modeling versus a linear elastic fracture mechanics approach*. Engineering Fracture Mechanics 75: 2842-2859.

Suo Z., Hutchinson J.W. (1990) *Interface crack between two elastic layers*. International Journal of Fracture 43:1-18.

Täljsten B. (1997) *Defining anchor lengths of steel and CFRP plates bonded to concrete*. International Journal of Adhesion and Adhesives 17:319-327.

Távara L., Mantič V., Graciani E., Cañas J., París F. (2010) *Analysis of a Crack in a Thin Adhesive Layer between Orthotropic Materials: An Application to Composite Interlaminar Fracture Toughness Test.* Computer Modeling in Engineering & Sciences 58:247-270.

Távara L., Mantič V., Graciani E., París F. (2011) *BEM analysis of crack onset and propagation along fiber–matrix interface under transverse tension using a linear elastic–brittle interface model.* Engineering Analysis with Boundary Elements 35:207-222.

Vaculik, J., Visintin, P., Burton, N.G., Griffith, M.C., Seracino, R. (2018a) *State-of-the-art review and future research directions for FRP-to-masonry bond research: Test methods and techniques for extraction of bond-slip behaviour.* Construction and Building Materials 183:325-345.

Vaculik J., Sturm A.B., Visintin P., Griffith M.C. (2018b) *Modelling FRP-to-substrate joints using the bilinear bond-slip rule with allowance for friction – Full-range analytical solutions for long and short bonded lengths*. International Journal of Solids and Structures 135:245-260.

Wu Y.F., Xu X.S., Sun J.B., Jiang C. (2012) *Analytical solution for the bond strength of externally bonded reinforcement*. Composite Structures 94:3232-3239.

Wu Y.-F., Jiang C. (2013) Quantification of bond-slip relationship for externally bonded FRP-to-concrete joints. Journal of Composites for Construction, 17:673-686.

Yuan, H., Wu, Z., Yoshizawa, H. (2001) *Theoretical solutions on interfacial stress transfer of externally bonded steel/composite laminates*. Structural Engineering/Earthquake Engineering, 18, 27-39.

Yuan H., Teng J.G., Seracino R., Wu Z.S., Yao J. (2004). *Full-range behaviour of FRP-to-concrete bonded joints*. Engineering Structures 26: 553-565.

Yuan H., Lu X., Hui D., Feo L. (2012) *Studies on FRP-concrete interface with hardening and softening bond-slip law*. Composite Structures 94:3781-3792.

Zhang W., Tang Z., Yang Y., Wei J. (2021) *Assessment of FRP-Concrete Interfacial Debonding with Coupled Mixed-Mode Cohesive Zone Model*. Journal of Composites for Construction, 25 (2), 04021002.

Zheng J.-J., Li Q.-B., Dai J.-G. (2020) *Analytical solution for FRP-to-concrete bonded joints considering local unloading and reloading.* Engineering Fracture Mechanics 235, 107185.

Zou X., Sneed L.H., D'Antino T., Carloni C. (2019) *Analytical Bond-Slip Model for Fiber-Reinforced Cementitious Matrix-Concrete Joints Based on Strain Measurements* Journal of Materials in Civil Engineering, 31 (11), art. no. 04019247.

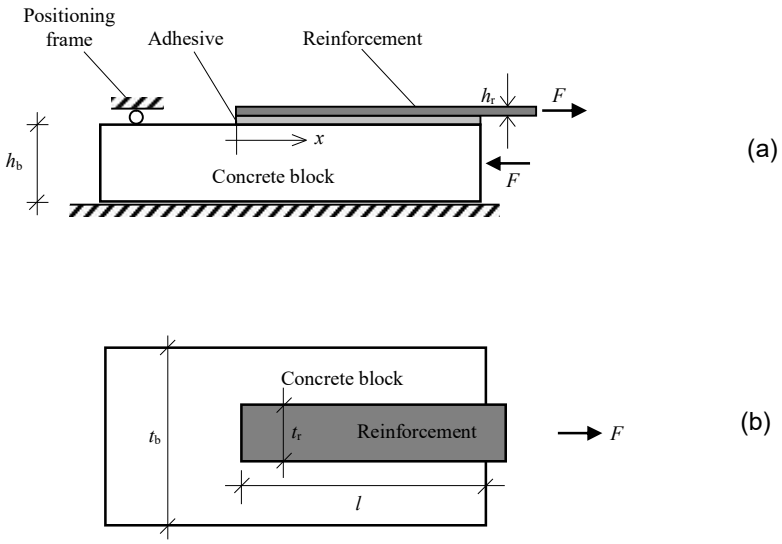

Figure 1. Single-lap shear test geometry: elevation (a), top view (b).

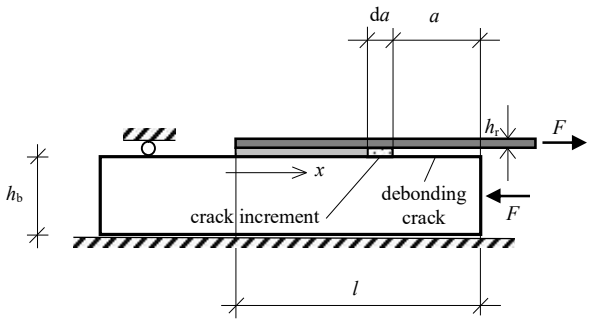

Figure 2. Debonding crack propagation.

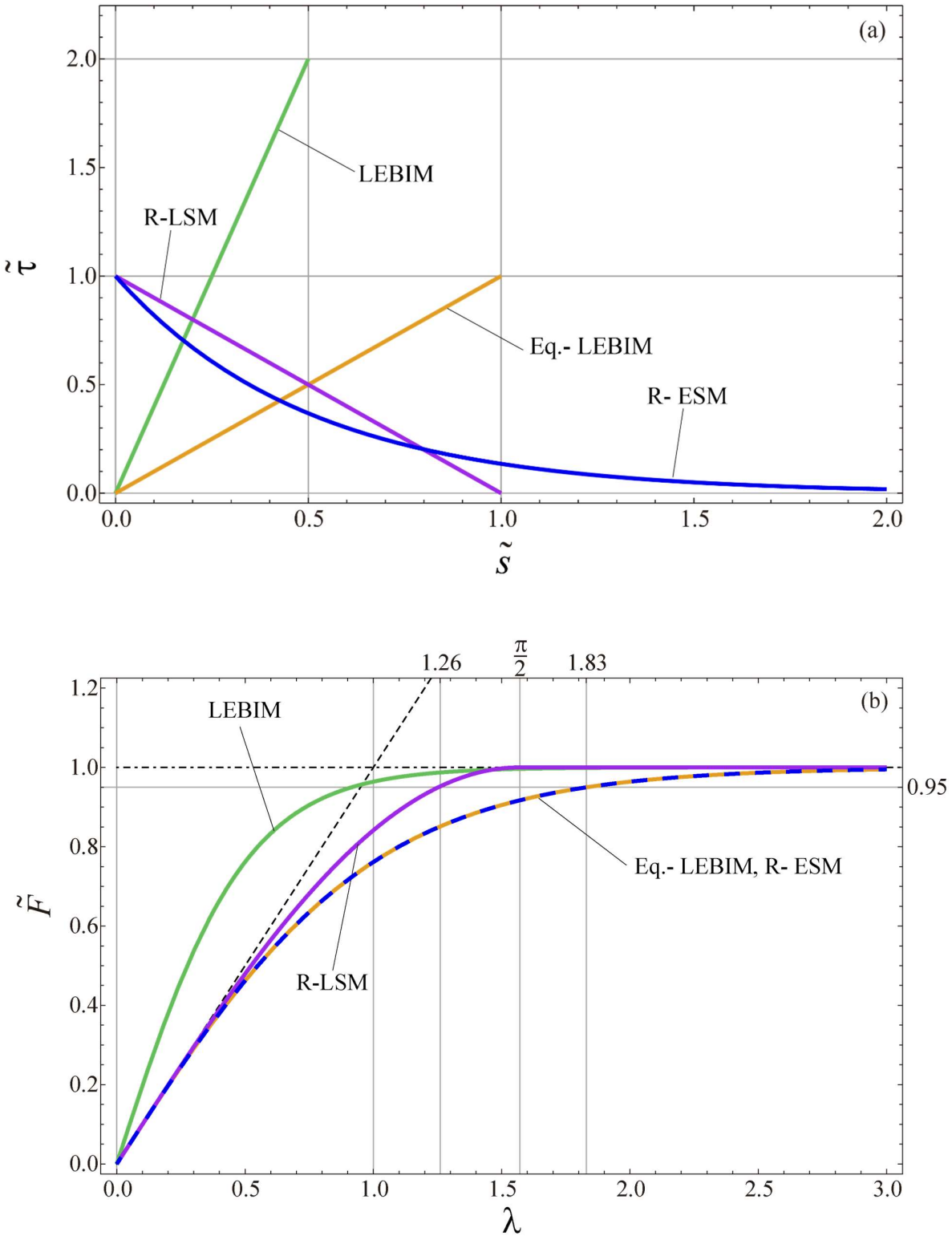

Fig. 3. Bond-slip law (a) and debonding load vs. bond length (b) according to two-parameter models. LEBIM curves refer to a μ value equal to 4. In (b): strength asymptote (dashed); energy asymptote (dot-dashed). Effective bond lengths are highlighted in (b), assuming β = 0.95. μ is defined in Eq. (45), λ and $\tilde{F}$ are defined in Eq. (22).

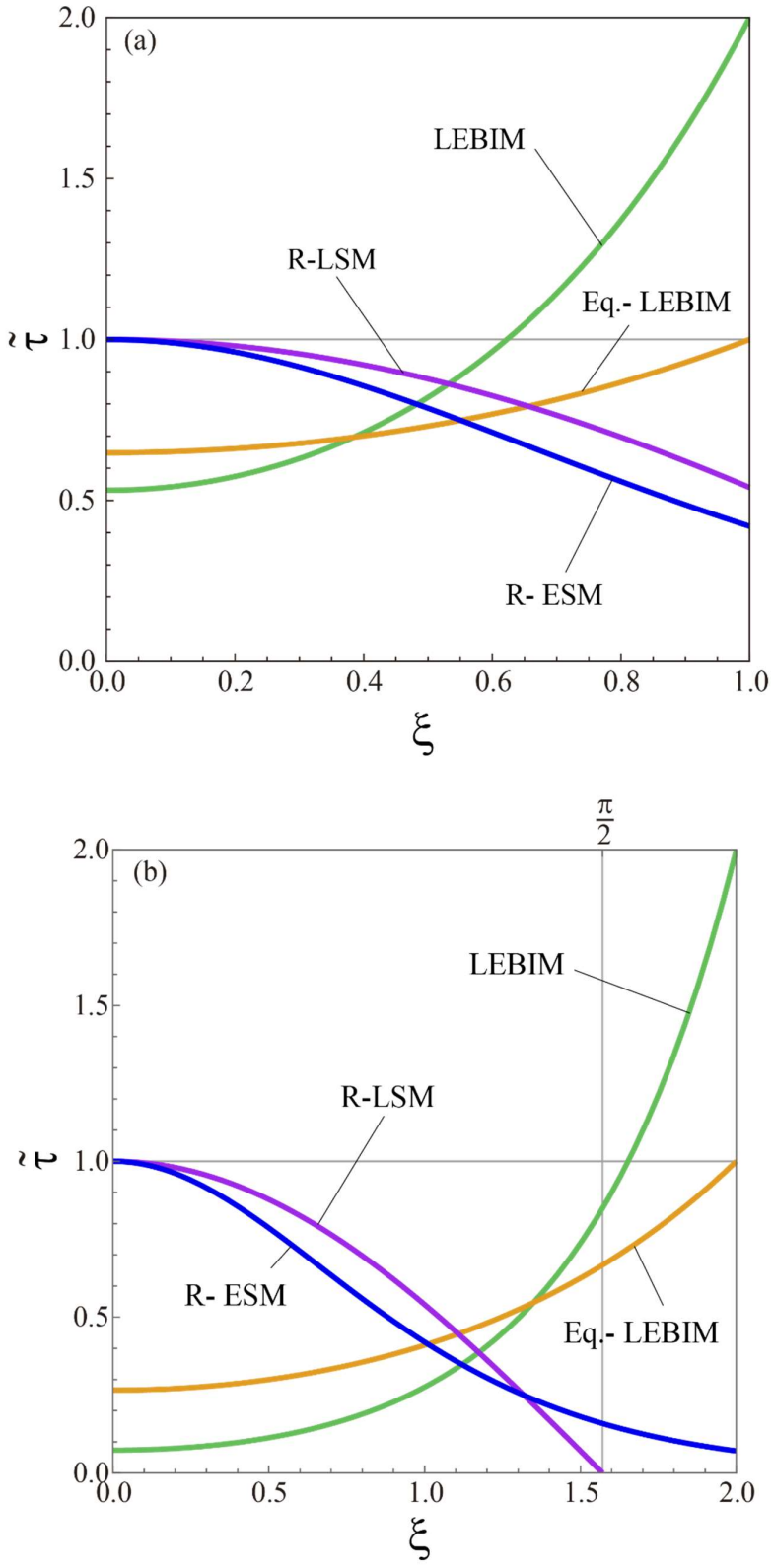

Fig. 4. Stress field at maximum load according to two-parameter models for overlap length $\lambda = 1$ (a) and $\lambda = 2$ (b). LEBIM curves refer to a μ value equal to 4 (as in Fig. 3). Underlying areas represent the debonding load; note that areas below Eq.-LEBIM and R-ESM curves are equal.

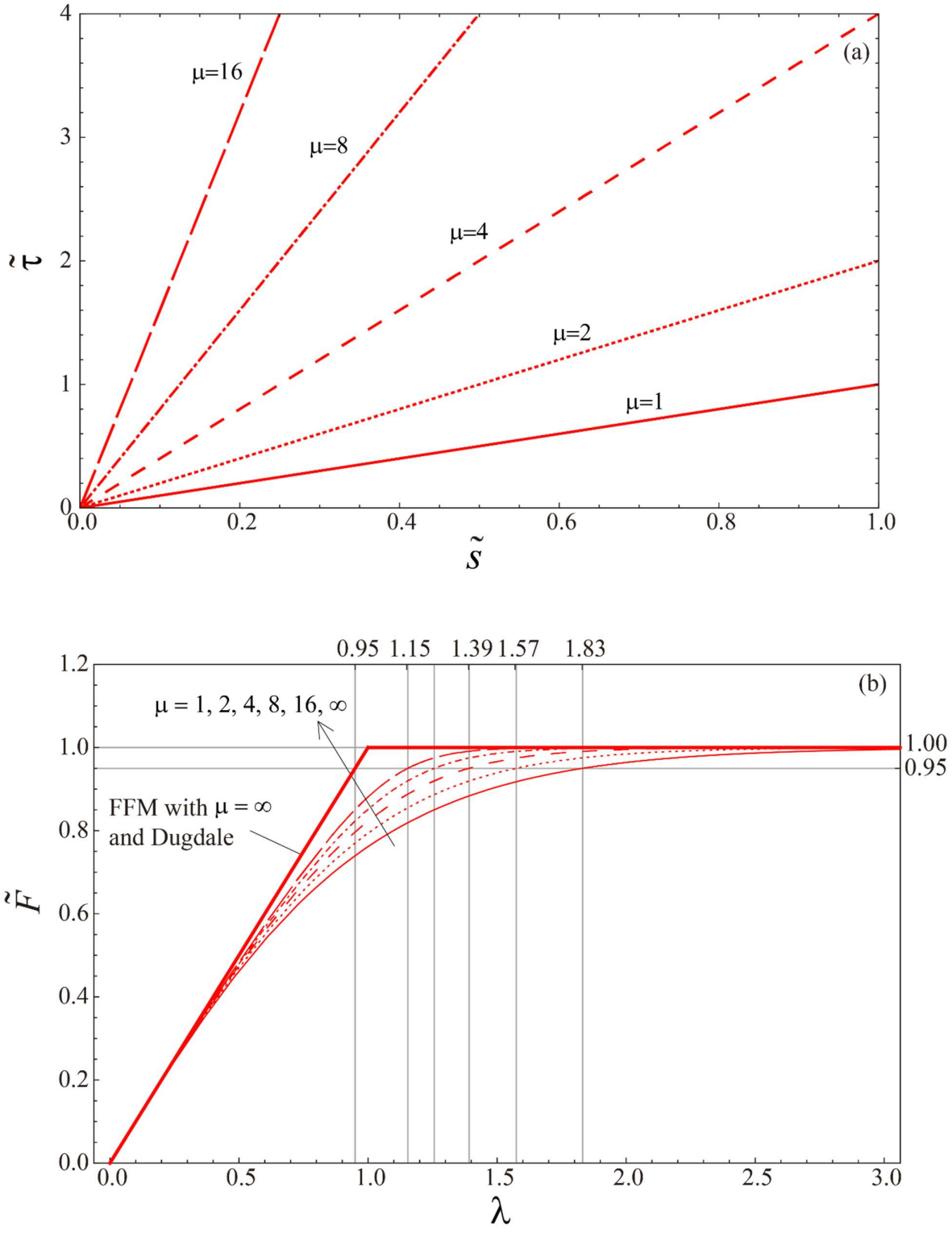

Fig. 5. Bond-slip law (a) and debonding load vs-bond length diagram (b) according to FFM. Different curves refer to different μ values. Thick line corresponds also to Dugdale model. Effective bond lengths are highlighted in (b), assuming β = 0.95.

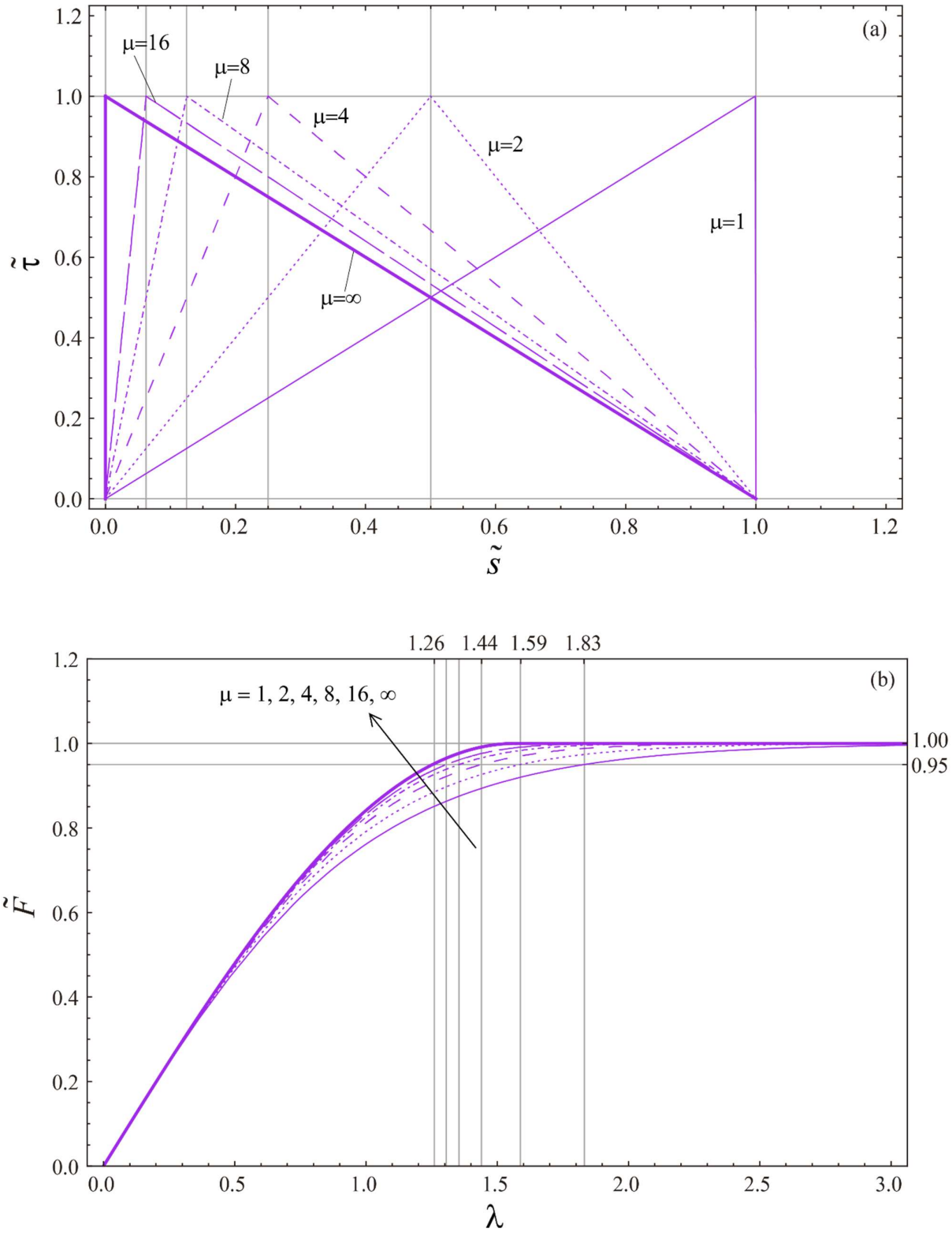

Fig. 6. Bond-slip law (a) and debonding load vs. bond length diagram (b) according to LE-LSM model. Different curves refer to different μ values. Effective bond lengths are highlighted in (b), assuming β = 0.95.

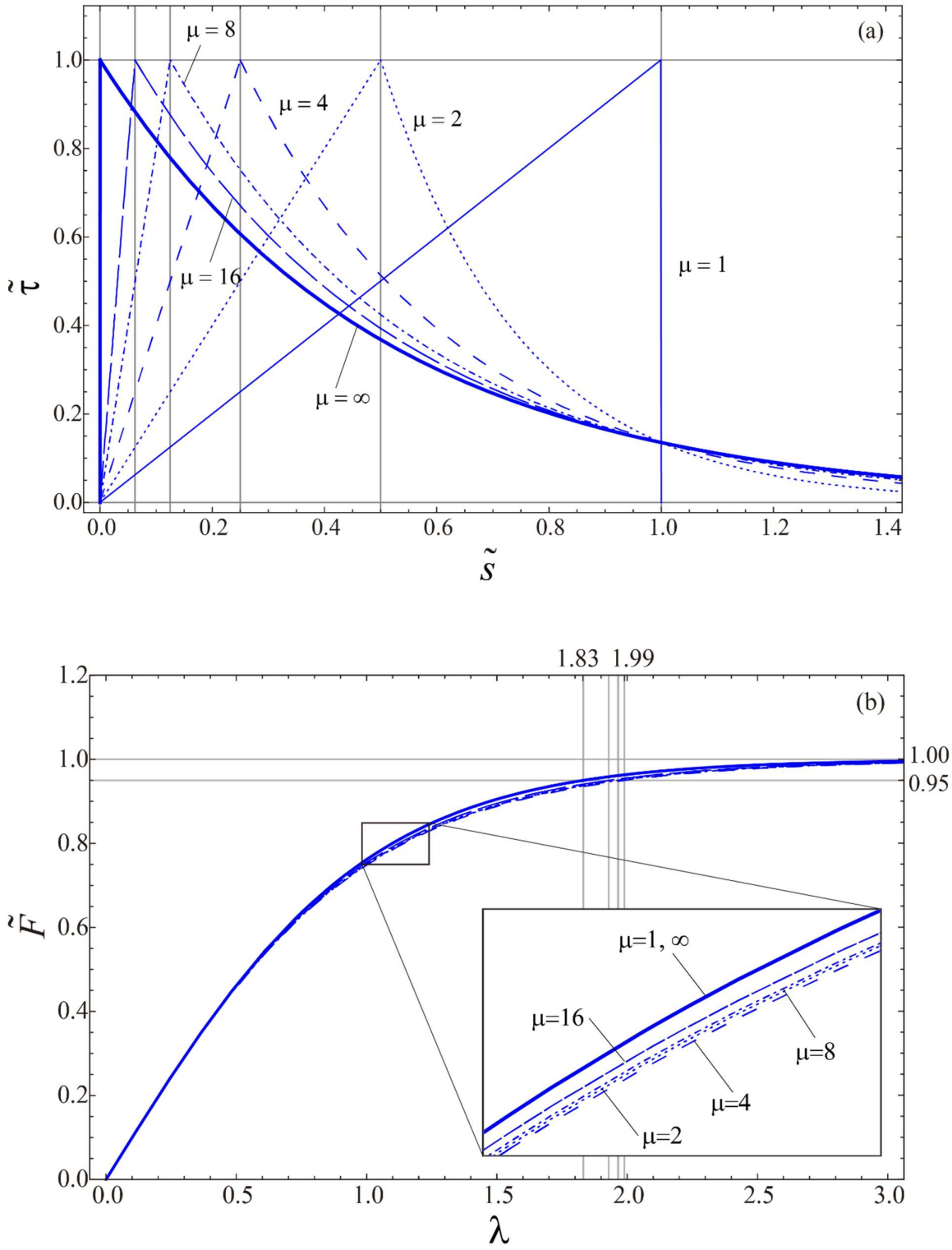

Fig. 7. Bond-slip laws (a) and debonding load vs- bond length diagram (b) according to the LE-ESM model. Different curves refer to different μ values. Effective bond lengths are highlighted in (b), assuming β = 0.95.

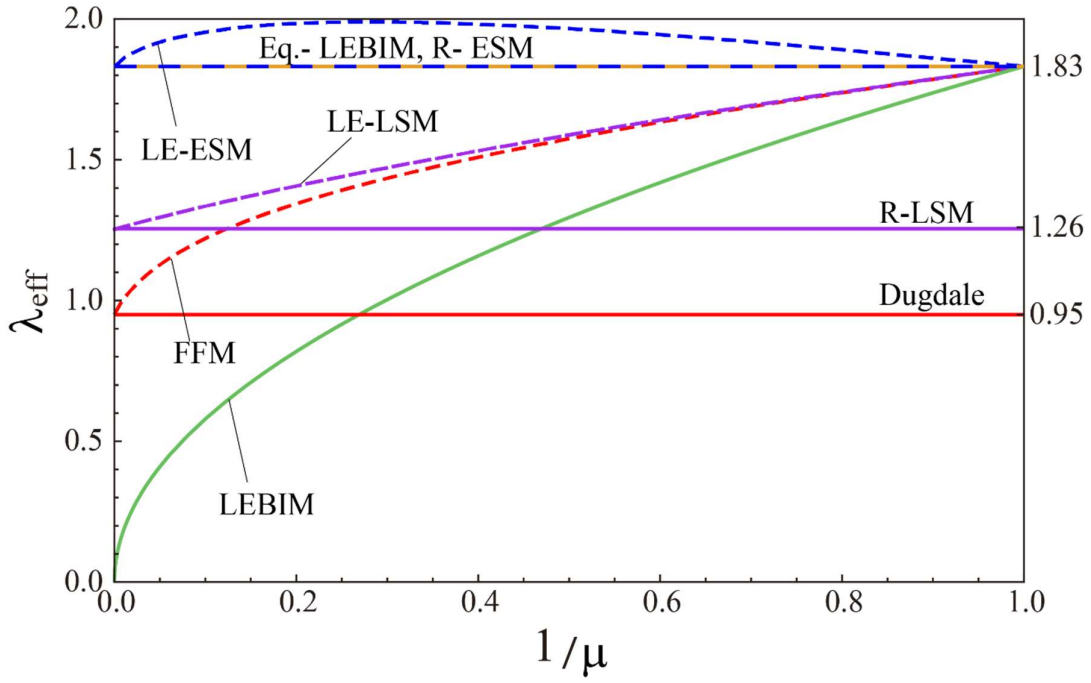

Fig. 8. Effective bond length vs. interface brittleness 1/μ (for β = 0.95). Continuous lines refer to 2-parameter models, dashed lines to 3-parameter model.

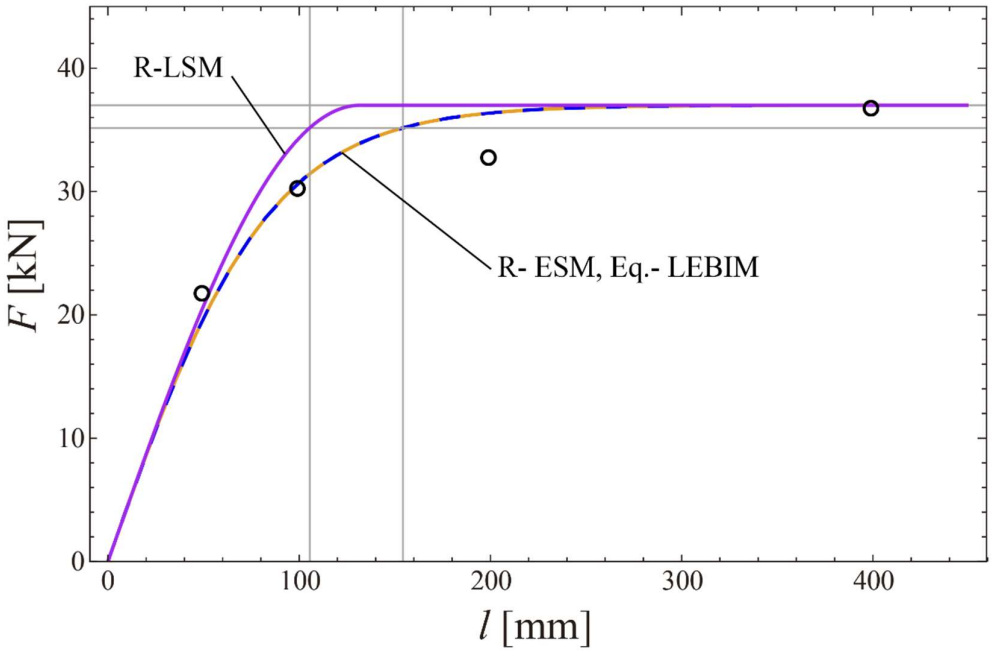

Fig. 9. Debonding load vs. bond length for the second series of experiments in Mazzotti et al. (2008).

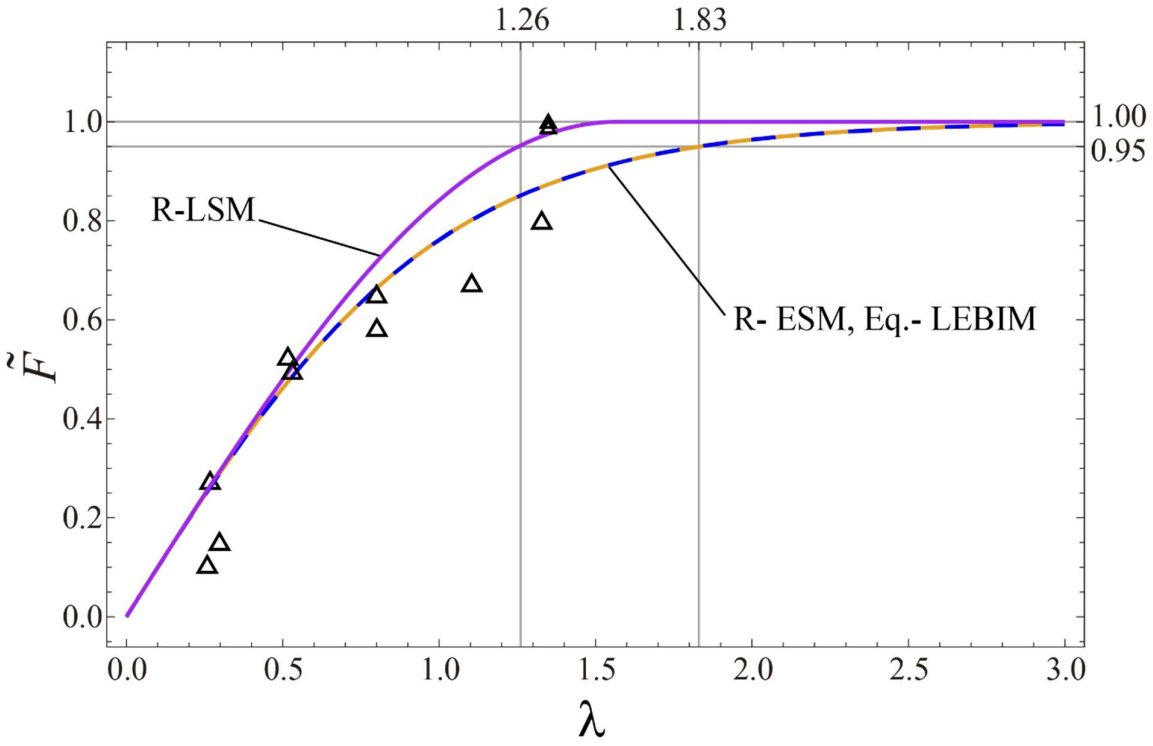

Fig. 10. Debonding load vs. bond length for the experiments by Carrara et al. (2011) in dimensionless form.

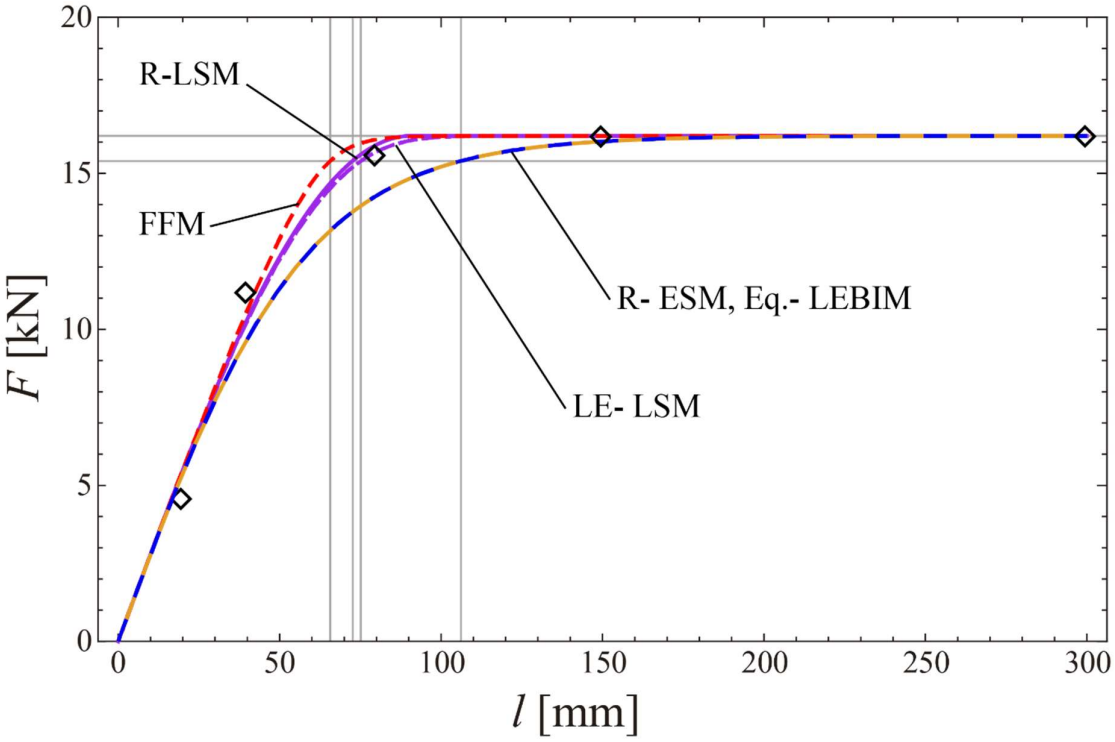

Fig. 11. Debonding load vs. bond length for the experiments by Dai et al. (2006), series 3.

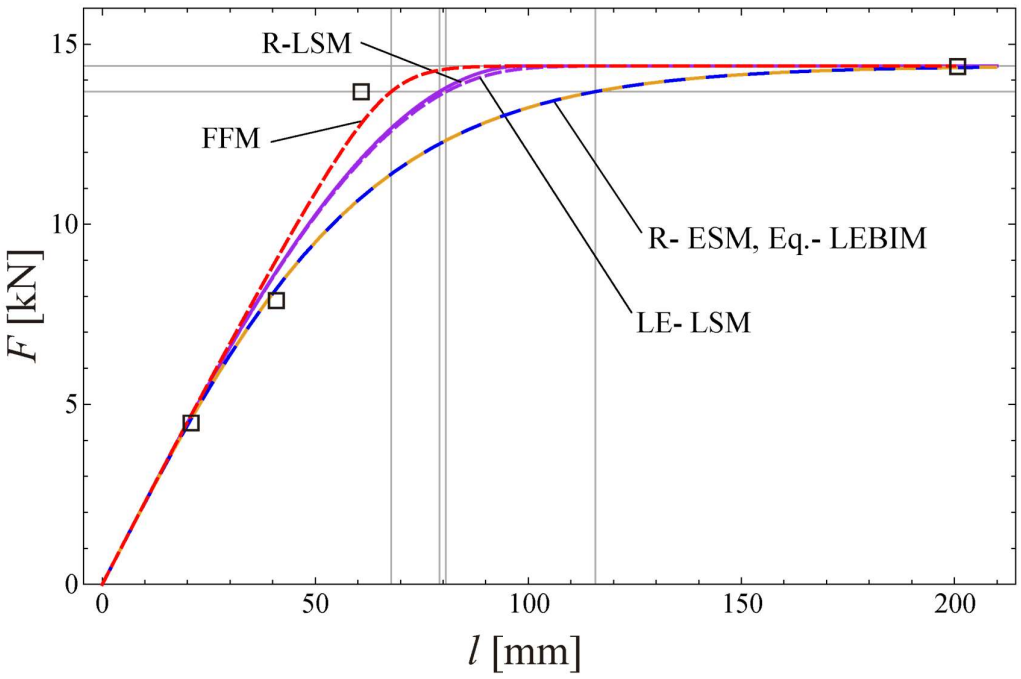

Fig. 12. Debonding load vs. bond length for the experiments by Dai et al. (2006), series 4.

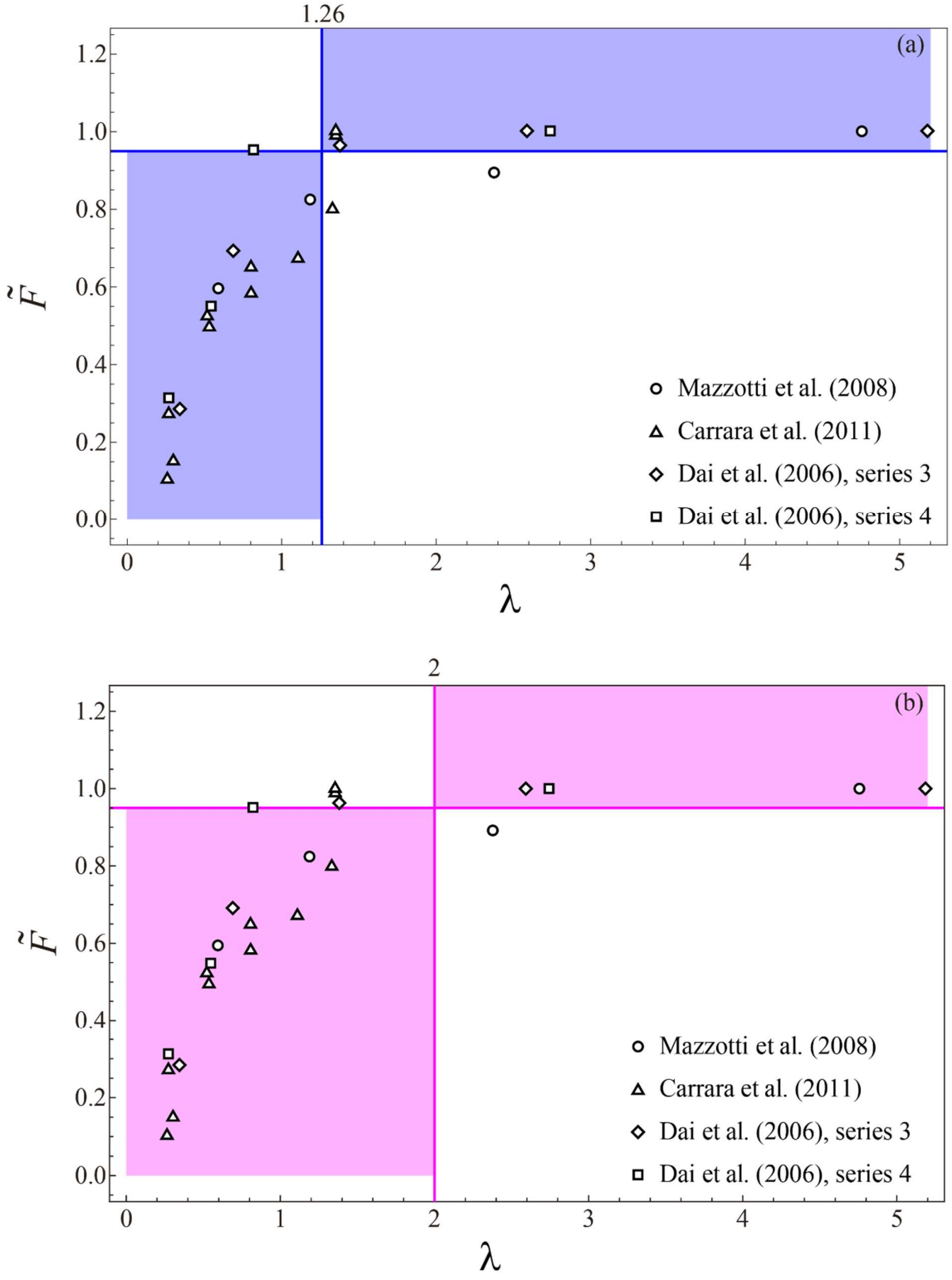

Fig. 13. Debonding load vs. bond length in dimensionless form for all the experimental data previously considered. Vertical lines represents the dimensionless effective length estimates, 1.26 in (a) and 2 in (b). Data in the shadowed area are data for which the estimate works; data outside are data for which estimate fails.